Master Research Project - MSc Physics

University of Groningen

Distributed qubit-register on a multi-node network with NV centers using Dynamical Decoupling with Radio Frequency pulses

Student:
Thomas Roelof Jan Fortuin

Supervisor:
Nicolas Demetriou (Daily)
dr. ir. Tim H. Taminiau
prof. dr. ir. Caspar Van Der Wal
prof. dr. Thomas (la Cour) Jansen

February 4, 2023

QuTech

Abstract

Future network-based quantum computation requires access to a large qubit register that can be controlled selectively and deterministically. A promising candidate for hosting quantum processors in such a network is the nitrogen-vacancy center (NV) in diamond. To expand the qubit register further, nuclear spins associated with carbon-13 atoms in the diamond can be used as an additional qubit resource in the network. Realizing large qubit register with these nuclear spins require gates that avoid crosstalk and protect the coherence of the system. This work exploits a novel method to selectively control nuclear spins using Dynamical Decoupling with Radio Frequency pulses (DDRF). The employment of a control field in this method to manipulate the state of the spin allows access to a large number of spins in the environment. We provide new insight and understanding of DDRF that addresses the driving efficiency. To optimize the gates, we built a model that estimates the gate fidelity of DDRF gates considering crosstalk and decoherence. We apply the optimized gates to a qubit-register distributed over a single-, two- and three- node network to create a Greenberger-Horne-Zeillinger (GHZ) state to estimate the performance of the register. We simulate the creation of a distributed GHZ-state of 7 qubits over two nodes with a fidelity of 0.55.

Contents

1 Introduction **1**

2 Theoretical background **3**
2.1 The NV center in Diamond . . . 3
2.2 Description of the total system of NV centre . . . 3
2.2.1 Optical interface . . . 5
2.3 Nuclear spin control . . . 5
2.3.1 Protecting decoherence using dynamical Decoupling (DD) pulses . . . 6
2.3.2 Dynamical Decoupling Radio Frequency (DDRF) . . . 6
2.3.3 Initialization . . . 7
2.4 Quantum Process Tomography (QPT) . . . 8
2.4.1 From a Quantum channel to the χ process matrix . . . 8
2.4.2 Error channels . . . 9

3 DDRF spectroscopy and global window suppression **11**
3.1 DDRF spectroscopy . . . 11
3.1.1 Harmonics of nuclear spin . . . 12
3.2 Global window . . . 13
3.2.1 Phase-track driving . . . 13
3.2.2 Motivation for the global window . . . 14
3.2.3 Approximate result of the global window function . . . 16
3.3 Conclusion . . . 16

4 Optimization of the DDRF gates **18**
4.1 Parameter space for DDRF-gates . . . 18
4.2 Decoherent noise sources . . . 19
4.2.1 Crosstalk . . . 19
4.2.2 Nuclear spin dephasing due to the spin-bath . . . 21
4.2.3 Electron coherence lifetime . . . 21
4.3 Estimation of the gate fidelity . . . 22
4.4 Conclusion . . . 25

5 Performance of the qubit-register **26**
5.1 Simulating the gates during the protocol . . . 26
5.2 Protocols . . . 27
5.2.1 Single node . . . 27
5.2.2 Two node network . . . 27
5.2.3 Three node network . . . 29
5.3 Conclusion . . . 29

6 Conclusion **30**

Acknowledgement **31**

A Appendix **32**
A.1 Table of nuclear spins . . . 32
A.2 Protection of electron coherence . . . 32
A.3 Harmonics . . . 34
A.4 Crosstalk . . . 35
A.5 Nuclear spin dephasing . . . 36
A.6 Gate fidelity . . . 37
A.7 Process matrix calculation in QuTip . . . 38
A.8 Remote-entanglement generation . . . 38
A.9 Controlling individual nuclear spins using dynamical decoupling . . . 39

Chapter 1

Introduction

The invention of the classical computer combined with Moore's law has triggered tremendous progress in the ability to compute industrial, social and scientific calculations [1]. However, there remains a set of problems for which the computation time on a classical computer scales exponentially with the input size of the problem, making it impossible to solve those problems in reasonable timescales. This has inspired research into the idea of the quantum computer, which potentially could solve a specific set of problems intractable for classical computers [2]. Whereas a classical computer consists of bits that can either be 0 or 1, the quantum mechanical counterpart of the bit, named qubit, can reside in a superposition of both. This, together with another quantum mechanical property, called entanglement, allows the quantum computer to solve some problems at an exponentially faster rate than the classical computer, resulting in potential applications in the fields of logistics, encryption, simulation of quantum mechancial systems for drug discovery, and other yet unknown areas [3] [4].

To realize quantum computation, many qubits that can be linked together are needed. A promising platform for a quantum processor is the nitrogen-vacancy center (NV) in diamond. This is a point defect in the diamond lattice hosting a spin system that can serve as a qubit. This qubit possesses an optical interface, which enables it to create entanglement links with other NV centers. In addition, the NV can interact with nuclear spins in its environment that belong to carbon-13 atoms in the diamond lattice. Selectively controlling these nuclear spins enables access to additional qubits within an NV node, resulting in a local qubit register. These two features could advance a network-based quantum computer, in which each node hosts an NV center as a quantum processor and a local qubit register of nuclear spins, see Fig. 1.1.

The nuclear spins of carbon-13 are an attractive candidate to expand the qubit register. They interact weakly with the environment and hence can have quantum states with long coherence times. The spins can also respond to external control fields making it possible to manipulate their states. Moreover, their unique interaction with the NV allows individual addressing of the spins. However,

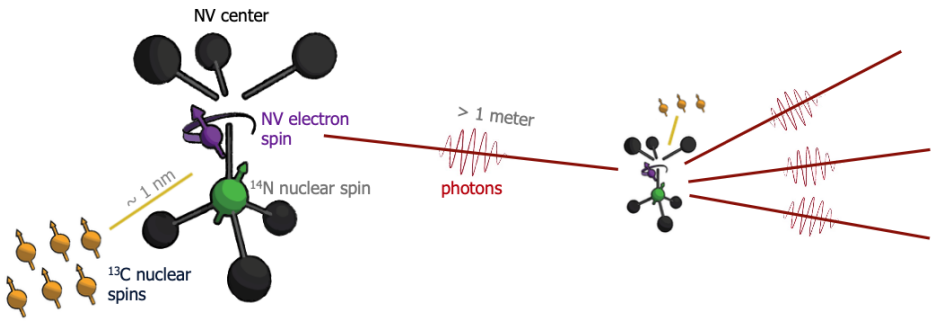

Figure 1.1: **Illustration of a distributed quantum computer.** Each node consists of an NV electron spin acting as a central qubit (purple), which can selectively control a qubit register of nuclear spins (yellow). The natural abundance of the carbon-13 atoms is 1.1%. In addition, the NV has an optical interface, enabling it to link with distant NV centers. Figure adapted from [5].

the abundance of the nuclear spins combined with the always-on hyperfine interaction also affects the NV spin, as the main source of decoherence for the NV is its interaction with nuclear spins. This makes the creation of large local qubit registers challenging.

To achieve good qubit control, Taminiau et al. 2012 [6] demonstrated the control of weakly-coupled nuclear spins while at the same time protecting the coherence of the NV spin. This method exploits specific interaction properties of the nuclear spin with the NV, imposing a limit to the number of accessible spins for the register. In this work, we exploit a novel method that controls the nuclear spin with an externally applied RF field while simultaneously decoupling the NV spin from interaction with its environment, the so-called dynamical decoupling with radio-frequency pulses (DDRF). This method selectively addresses nuclear using a control field, therefore increasing the number of accessible spins. Bradley et al. [7] has demonstrated a ten-qubit register exploiting this method.

This work provides new insight in the driving efficiency of DDRF and aims to expand the qubit register by optimizing the gates. We first characterize the nuclear spins in an NV center using DDRF spectroscopy. Next, we address an observation in Bradley et al. 2019 [7] and provide a qualitative argument for this using the so-called global window suppression, essential for designing DDRF gates and imaging the parameter space. To create a large qubit register, quantum gates that avoid crosstalk and protect the overall coherence of the register are needed. We simulate the effect of these decoherence sources on the DDRF gates, allowing us to obtain the high-fidelity gates. Employing these optimized gates, we investigate the performance of the qubit register by creating a Greenberg-Horne-Zeillinger (GHZ) state with an increasing number of qubits. Moreover, following the demonstration of a multi-node network in Pompili et al. 2021 [8], we explore the performance of the register distributed over multiple nodes and establish a distributed GHZ state. The potential to scale the qubit register in a network fashion will allow future demonstrations of distributed quantum computing.[9]

Chapter 2 provides the theoretical foundation of this work. We introduce the NV center in diamond that serves as the central qubit. Next, we describe the technique to control the nuclear spins surrounding the NV spin with DDRF. To eventually characterize and optimize the gates, we use quantum process tomography, which provides a representation of the process in the form of a process matrix. This enables us to estimate the fidelity of the gates.

In **Chapter 3**, we characterize the nuclear spins that constitute the local spin register and build on the understanding of the DDRF signals. Ref. [7] has observed a suppression of the driving efficiency of DDRF for different nuclear spins. Here we try to elaborate on this finding by introducing a suppression function to the driving of DDRF, which we call the global window suppression. Understanding of this effect is essential for designing the gates.

Chapter 4 discusses the optimization of the DDRF gates. We examine in more detail the parameter space of DDRF such that we can obtain the desired operations. To ensure gates that avoid crosstalk and protect the coherence of the register, we investigate the effect of decoherent noise sources on these gates. Subsequently, we can characterize the high-fidelity gates for each spin in the register.

Chapter 5 investigates the performance of the qubit register by creating GHZ states with an increasing number of qubits. For this, we design a model that applies the two-qubit gates obtained in Ch. 4 within a circuit and considers the noise sources to give a realistic insight into the performance. Following the demonstration of a multi-node quantum network in Ref. [8], we investigate the setups in which the qubit register is on a single node and distributed on a network.

Finally, in **Chapter 6**, we summarize our findings and discuss future steps.

Chapter 2

Theoretical background

In this Chapter, we present the theoretical background of this work. First, we present the NV center, acting as the central qubit within a node. Next, we describe the techniques to operate the nuclear spins surrounding the NV, which are employed as additional qubits in the register. Finally, we introduce the process matrix formalism in quantum process tomography, which enables us to characterize and optimize the DDRF gates in Ch. 4, as well as to execute protocols that reflect the performance of a register in Ch. 5.

2.1 The NV center in Diamond

The NV center is a point defect in diamond where two neighbouring carbon atoms are substituted for one nitrogen atom (N) and a vacancy (V). By capturing an extra electron from its environment, the defect becomes negatively charged, resulting in NV^-. The ground level of the electron spin of the NV centre is a spin-1 system and it will serve as the central qubit. An important property of the NV centre, is that the ground and first excited electronic energy levels are within the diamond bandgap and are unoccupied for the negative charge state. This gives the NV centre an optical interface, with the optical transitions between the two energy levels being mostly cyclic which can be used for read-out, initialization and remote entanglement generation of the electron spin, as will be discussed later.

In a non-purified diamond, the natural abundance of the ^{13}C isotope (which is a spin-1/2 system) is 1.1%. This results in a nuclear spin-bath surrounding and continuously interacting with the electron spin. Previous work has shown that it is possible to resolve and address individual nuclear spins from the spin-bath. This allows the nuclear spins to be exploited as a possible additional qubit resource within the NV node, therefore resulting in a qubit register. A schematic overview of the NV node is depicted in Figure 1.1.

2.2 Description of the total system of NV centre

As introduced above, the diamond that hosts the NV electronic spin consists of other components as well: ^{13}C atoms and ^{14}N atoms, that possess a nuclear spin-1/2 and spin-1, respectively. These nuclear spins interact with the electron spin. The total description of the system is described by a summation of all the components of the system:

$$H = H_e + H_N + H_C + H_{e,N} + H_{e,C} + H_{C,C} + H_{N,C}, \tag{2.1}$$

where H_e is the NV electronic spin ground state Hamiltonian, $H_N(H_C)$ is the ^{14}N(^{13}C) nuclear spin Hamiltonian, $H_{e,N}$ is the interaction Hamiltonian of the hyperfine interaction between the electron spin and nitrogen nuclear spin, $H_{C,C}$ is the nuclear-nuclear interaction between the ^{13}C nuclear spins, $H_{N,C}$ is the interaction Hamiltonian between the electronic spin and nitrogen nuclear spin.

Electronic ground state

The energy levels of the electronic spin are depicted in Fig. 2.2. The $^3A_2$ ground state of the electronic spin is split into two levels with zero-field splitting of $D_{GS} \approx 2.88$ GHz. By applying an external

magnetic field $\vec{\mathbf{B}}$, the degeneracy of the $m_s = \pm 1$ is split further due to the Zeeman effect. This gives rise to the following ground-state Hamiltonian of the electron spin (neglecting strain-interaction, since this is generally weak in the ground state):

$$H_e = D_{GS} S_z^2 + \gamma_e \vec{\mathbf{B}} \cdot \vec{\mathbf{S}}, \tag{2.2}$$

where $\gamma_e \approx 2.8$ MHz/G is the electron gyromagnetic ratio and $\vec{S}$ are the spin-1 Pauli operators. In our case, the magnetic field is applied along the z direction of the symmetry axis. This three-level energy splitting allows us to define our qubit subspace in $m_s = 0(-1)$ that act as $|0\rangle$ ($|1\rangle$). By applying microwave pulses resonant with the transition frequency it is then possible to selectively drive the qubit state.

^{14}N nuclear spin

The neighbouring ^{14}N nuclear spin is a spin-1 system that couples strongly to the electron spin. The Hamiltonian of the nuclear spin and its interaction with the electron spin is given by:

$$H_N + H_{e,N} = -Q_N I_{N,z}^2 + \gamma_N \vec{\mathbf{B}} \cdot \vec{\mathbf{I}}_N + \vec{\mathbf{S}} \cdot \vec{\mathbf{A}}_N \cdot \vec{\mathbf{I}}_N, \tag{2.3}$$

where $Q_N \approx 4.98$ MHz is the quadruple splitting of the nitrogen, γ_N is its gyromagnetic ratio, $\vec{\mathbf{A}}_N$ is the hyperfine tensor, and $\vec{\mathbf{I}}$ are the spin-1 operators. Under the secular approximation, the last term is approximated by $A_\parallel \hat{S}_z \hat{I}_{N,z}$, where $A_\parallel \approx 2.16$ MHz is the parallel component of the hyperfine interaction, introducing the electron state to split into three levels. The strong coupling between the nitrogen and electron spin can impose a problem when storing quantum information on the nitrogen spin. While controlling the electron spin, this will affect the state of the nuclear spin and therefore distort the information stored in it. This imposes a limit on the ability of the nitrogen spin to store quantum information and be used in the qubit register.

To ensure that electron spin control does not become conditional on the nitrogen spin state if the nitrogen is uninitialized, the applied MW pulse should be broad enough in frequency space to cover all the three energy splittings of the electron spin due to the coupling with the nitrogen spin. Applying short pulses such that the frequency response is broad will address the three peaks separated by 2.16 MHz.

^{13}C nuclear spins

The ^{13}C nuclear spins surrounding the NV center constitute a spin-1/2 system. The Hamiltonian for one ^{13}C nuclear spin and an electronic spin is given by:

$$H_C + H_{e,C} = \gamma_C \vec{\mathbf{B}} \cdot \vec{\mathbf{I}} + \vec{\mathbf{S}} \cdot \vec{\mathbf{A}}_N \cdot \vec{\mathbf{I}}_N, \tag{2.4}$$

where $\gamma_C = 1.0705$ kHz/G is the carbon nuclear spin gyromagnetic ratio, $\vec{\mathbf{I}}$ are the spin-1/2 operators for the nuclear spin and $\vec{\mathbf{A}}$ is the hyperfine tensor describing the electron-^{13}C interaction. As the gyromagnetic ratio is three-orders of magnitude smaller than for the electron spin, the nuclear spin can have a much longer coherence time.

Within the secular approximation, this Hamiltonian can be rewritten as follows:

$$H = \omega_L I_z + A_\parallel S_z I_z + A_\perp S_z I_x, \tag{2.5}$$

where $\omega_L = \gamma_c B_z$ is the Larmor precession frequency of the nuclear spin around the external magnetic field applied along the z-axis of the NV, $A_\parallel (A_\perp)$ are the parallel (perpendicular) hyperfine interaction couplings between the electron and nuclear spin when the electron is in the $m_s = -1$ and S and I are the electron (spin-1) and nuclear (spin-1/2) operators, respectively.

By an appropriate basis rotation, Eq. 2.5 can be rewritten into:

$$H = |0\rangle\langle 0| \otimes H_0 + |1\rangle\langle 1| \otimes H_1 \tag{2.6}$$

$$H_0 = \omega_L I_z \tag{2.7}$$

$$H_1 = (\omega_L - A_\parallel) I_z + A_\perp I_x. \tag{2.8}$$

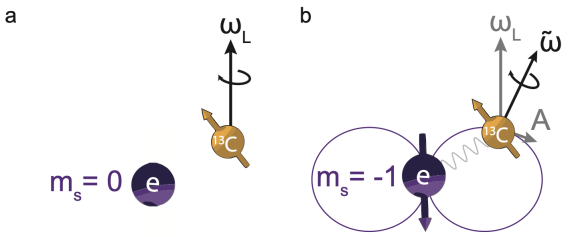

Figure 2.1: **^{13}C nuclear spins hyperfine interaction with electron spin.** (a) When $m_s = 0$, there is no hyperfine interaction and the nuclear spin rotates along the external magnetic field with Larmor frequency ω_0. (b) When $m_s = -1$, hyperfine interaction is turned on and the precession frequency is adjusted: $\omega_1 = \sqrt{(\omega_L - A_\parallel)^2 + A_\perp}$, where the rotation is axis is tilted due to presence of $A_\perp$. Figure adapted from Ref. [10].

The key result here is that the hyperfine interaction induces a dependency on the initial electron spin eigenstate to the precession frequency and rotation axis of the nuclear spin. In $m_s = 0$, the nuclear spin precesses around the external magnetic field with frequency ω_L. When the electron spin is in $m_s = -1$, the nuclear spin precesses with the generalized frequency $\omega_1 = \sqrt{(\omega_L - A_\parallel)^2 + A_\perp^2}$ and the rotation axis is tilted depending on $A_\perp$. This is depicted in Figure 2.1.

In addition to these interactions, there are also interactions between neighbouring ^{13}C nuclear spins. However, since these are of the order of a few to ten Hz and hence very weak compared to previously described interactions. Within the typical gate times that we are working with (1 ms), we therefore assume these interactions are negligible.

2.2.1 Optical interface

At cryogenic temperatures, the ground state can be excited resonantly to the different ^3E excited states, as shown in Fig. 2.2. Due to the cyclic behaviour of some of these transitions, it is possible to create spin-photon entanglement that allows for read-out, initialization and creation of remote-entanglement links.

The transition $m_s = -1 \leftrightarrow |E_{1,2}\rangle$ is used for initialization of the electron spin in $m_s = 0$. This transition decays back via the singlet state to $m_s = 0$ with a small probability, but by applying this selective pulse long enough, the electron spin initializes in $m_s = 0$.

Additionally, the transition $m_s = 0 \leftrightarrow |E_{x,y}\rangle$ is used for read-out of the NV state and creation of remote-entanglement. This transition is spin-preserving and separated by 1.945 eV (637 nm). These resonantly emitted photons are within the zero-phonon line (ZPL). Unfortunately, only 3% of the emitted light is coming from the ZPL that can be used for remote entanglement. The vast majority is emitted by off-resonant photons accompanied by a phonon. This forms the phonon-sideband (PSB) and the light emitted from this breaks the spin-preservation between the collected photon and the electron spin, and therefore cannot be used for remote entanglement. To establish a remote entanglement link between two distant NV centers, we consider the single-photon protocol used in Ref. [8], which is described in App. A.8

2.3 Nuclear spin control

To create qubit registers within an NV node, we need local two-qubit gates that entangle the electron and nuclear spin. As the electron and nuclear spins have a hyperfine interaction, this can be used to control the nuclear spins. However, this always-on interaction with the environment also causes the electron spin to lose coherence. First, we describe the protection of electron spin coherence using dynamical decoupling sequences. Next, we introduce the dynamical decoupling with radio frequency pulses used to create conditional gates.

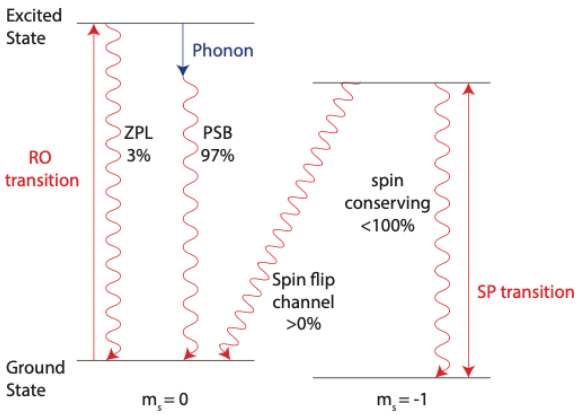

Figure 2.2: **Energy levels of the NV electron spin**. Read out (RO) transitions between $m_s = 0$ and excited state $E_{1,2}$ can happen resonantly (i.e. ZPL), which can be used for remote entanglement, or off-resonanlty in the phonon side band. The spin-pumping (SP) transition happens between $m_s = -1$ and $A_{1,2}$, which decays back to $m_s = 0$ with a non-zero probability. Repeated exciting this transition will eventually transfer the population form $m_s = -1$ to $m_s = 0$. Acknowledgements to S.J.H. Loenen.

2.3.1 Protecting decoherence using dynamical Decoupling (DD) pulses

Besides the strong coupled nuclear spins, there is also a large number of weakly coupled nuclear spins, forming the nuclear spin-bath. Due to their weak coupling, the probability of a flip-flop interaction between two spins is high, inducing a time-varying spin configuration of the spin-bath. This induces a quasi-static fluctuation of the magnetic field felt by the electron spin and dephases the electron spin when in a superposition state.

To cancel this effect, sequential π-pulses on the electron with an interpulse delay of τ are applied to the electron. If the time between the pulses is short relative to the fluctuation of the magnetic field, the dephasing before the spin-flip mirrors the dephasing after the spin flip, hence the dephasing is echoed out. This way the electron coherence can be protected over long times by applying sequential DD pulses, however, eventually will also undergo a decay characterized by the T_2 time.

Moreover, it can be shown that by setting the interpulse delay to a specific resonance, the electron spin can interact with an individual nuclear spin and therefore control the nuclear spin, which is based on the specific dynamical properties of the nuclear spin (i.e. $A_\perp$), see App. A.9 [6].

2.3.2 Dynamical Decoupling Radio Frequency (DDRF)

In this work we create conditional gates by applying phase-controlled radio frequency (RF) driving of the nuclear spin interleaved with dynamical decoupling sequences, the so-called DDRF gate.

In addition to the interaction Hamiltonian shown in Eq. 2.5, in the presence of an RF field there is an extra term describing the interaction between the driving field and the nuclear spin:

$$H_{\mathrm{RF}} = 2\Omega \cos(\omega t + \phi) I_x, \tag{2.9}$$

where the RF field is oscillating along the x-axis with frequency ω, phase ϕ and Rabi frequency Ω.

For simplicity, we will first consider $A_\perp = 0$, meaning that the quantization axis lies along the Z-axis for $m_s = -1$ (i.e. no tilting of the rotation axis). The precession frequency is then adjusted with $\omega_1 = \omega_L - A_\parallel$. In the rotating frame at frequency ω with the use of the rotating wave approximation, the Hamiltonian becomes:

$$H = |0\rangle\langle 0| \otimes (\omega_L - \omega_1) I_z + |1\rangle\langle 1| \otimes (\omega_1 - \omega) I_z + \Omega(\cos(\phi) I_x + \sin(\phi) I_y). \tag{2.10}$$

By setting the RF frequency resonant with the $m_s = -1$ nuclear spin precession frequency (i.e. $\omega = \omega_1$) and in case of far nuclear spin detuning from the Larmor precession (i.e. $\omega_L - \omega_1 \gg \Omega$), the interaction Hamiltonian becomes (after neglecting non-secular terms, i.e. very fast oscillating terms):

$$H = |0\rangle\langle 0| \otimes (\omega_L - \omega_1) I_z + |1\rangle\langle 1| \otimes \Omega(\cos(\phi) I_x + \sin(\phi) I_y). \tag{2.11}$$

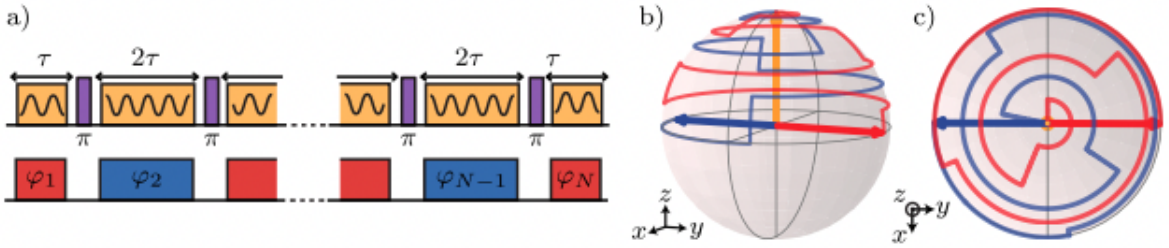

Figure 2.3: **DDRF sequence**. (a) Pulse sequences corresponding to a DDRF sequence. Yellow indicates RF pulses with corresponding phases ϕ below for even(blue) and odd(red) pulses, corresponding to phases calculated with Eq. 2.12. Purple indicates the π-pulses on the electron spin, with a MW pulse. (b,c) Depicting the evolution of a nuclear spin initially in $|0\rangle$ (yellow arrow) during a DDRF sequence for initial electron states $m_s = 0$ (red) and $m_s = -1$ (blue). Figure adapted from Ref. [7].

This shows that under RF driving, in the case of $m_s = 0$ the nuclear spin precesses around the z-axis with frequency $A_\parallel$ and when $m_s = -1$, the nuclear spin will rotate in the $x-y$ plane depending on the phase of the RF field. By setting the RF frequency resonant with a particular nuclear spin precession frequency, we selectively drive nuclear spins.

To protect the electron spin from decoherence by coupling to the spin bath, the RF pulses are interleaved with DD sequences: $(\tau - \pi - 2\tau - \pi - \tau)^{N/2}$. By toggling between the eigenstates of the electron spins and adjusting the phase of the RF pulse after each pulse, this will induce different evolutions for both initial eigenstates of the electron spin. When initially in $m_s = 0(-1)$, only the even (odd) RF pulses will be resonant, and therefore induce a rotation on the nuclear spin.

To make sure that the rotations during each RF sequence builds up constructively, the phase should be adapted for the accumulated phase during free precession. These are integer multiples of $\phi_\tau = (\omega_0 - \omega_1)\tau$. Therefore the required phase for the k-th RF pulse is given by:

$$\phi_k = \begin{cases} \phi + (k-1)\phi_\tau + \pi, & \text{for } k \text{ odd} \\ \phi + (k-1)\phi_\tau, & \text{for } k \text{ even}, \end{cases} \tag{2.12}$$

where ϕ is the phase that sets the rotation axis and the extra π shift ensures that the nuclear spin rotations build up to a conditional rotation on the initial electron eigenstates.

The final result of these phases is a total evolution of the two-qubit system given by $V = V_z \cdot V_{\text{CROT}}$, which constitutes an unconditional (first term) and a conditional (second term) rotation on the nuclear spin. The conditional term is given by:

$$V_{\text{CROT}} = |0\rangle\langle 0| \otimes R_\phi(N\Omega\tau) + |1\rangle\langle 1| \otimes R_\phi(-N\Omega\tau), \tag{2.13}$$

where $R_\phi(\theta) = e^{-i\theta(\cos(\phi)I_x + \sin(\phi)I_y)/\hbar}$. In order to obtain a maximally entangling two-qubit gate between the electron and nuclear spin, the parameter must be set by $N\Omega\tau = \pi/2$. This condition is, however, an approximation and later in this work we show when it breaks down. Eventually, the created two-qubit gate is related to a CNOT-gate up to single-qubit rotations.

In the above derivation, we have set $A_\perp = 0$. Introducing a non-zero $A_\perp$, this will enforce the nuclear spin to precess along tilted quantization axes with respect to different electron spin eigenstates. In this work, we simulate the unitary evolution operators of the DDRF gates.

2.3.3 Initialization

Before doing quantum logic operations on the qubits, the spin-states need to be initialized in a known state. There are two ways to initialize: in a probabilistic (measurement-based (MBI)) or deterministic (SWAP) way. In this work, we use SWAP, see Fig. 2.4. The goal is to swap the state of the electron to the nuclear spin.

The initial state at the start is the electron spin in the state $|0\rangle$ and the nuclear spin in a completely mixed state (since $k_bT \gg \hbar\gamma B_z$) which is written as $\rho = (|0\rangle\langle 0| + |1\rangle\langle 1|)/2$. Applying a $\pi/2$-rotation around x to the electron spin brings it into a superposition state. When the two-qubit gate is applied,

the electron spin accumulates a $\pi/2$ phase depending on the nuclear spin state. This phase shift is then accounted for with the $\pi/2$-rotation around x on the electron spin, bringing the electron spin to the computational basis. Next, a controlled $\pi/2$-rotation around y is applied to the nuclear spin, resulting in the nuclear spin ending up in $|0\rangle$ independent of the state of the electron spin. Finally, the electron spin gets reset by spin-pumping.

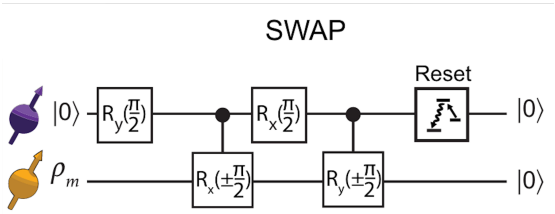

Figure 2.4: **SWAP initialization.** The protocol to initialize the nuclear spin (yellow) into the $|0\rangle$ state using SWAP, where the electron spin (purple) is in $|0\rangle$ state by spin-pumping. The two-qubit gates are conducted by DDRF or DD. Figure adapted from Ref. [10].

2.4 Quantum Process Tomography (QPT)

To characterize and optimize the DDRF gates, we need a full description of the unitary evolution of DDRF gate, which is the process matrix. Applying a DDRF gate affects the quantum state, and the χ process matrix can characterize this process. However, influence from the environment will induce imperfections to this process and therefore affect the process fidelity. First we will introduce the object χ. Then we will describe common ways to model processes that are due to the errors. Finally, we show how this can help us to determine the fidelity of a gate.

2.4.1 From a Quantum channel to the χ process matrix

In general, a quantum state can undergo many processes that alter the state of the quantum system, ranging form a unitary transformation, non-unitary transformation or interaction with its environment, and all these processes can be described by a quantum channel. A quantum channel ε is a linear map from an input state ρ_{in} to a final state ρ_{final}, $\varepsilon(\rho_{\text{in}}) = \rho_{\text{final}}$, and therefore acts as a map between Hilbert spaces. This can be generalized to systems with larger number of qubits by taking the tensor product. The quantum channel can then for example act on a subset of the Hilbert space, while idle on the rest of the system (i.e. applying an Identity operation).

Since a quantum channel is a map from physical quantity to another physical quantity (i.e. the density matrices), this imposes two constraints on the map: complete-positivity (CP) and trace-preservation (TP). CP must hold to ensure that the density matrix after the channel is positive-semidefinite (i.e. non-negative eigenvalues), even if the channel acts on a subset of the system [11]. Furthermore, for a normalized state it follows that the trace of the density matrix is required to be unity. Therefore, in order for the final state after the channel to also be normalized, the channel is required to preserve the trace.

To characterize a quantum process, we use Quantum Process Tomography (QPT). The goal of QPT is to give a representation of the quantum process induced by a quantum channel and in this Thesis, we work with the χ process matrix. This matrix describes a decomposition of the quantum process in an orthogonal operator basis and therefore completely characterizes the quantum channel ε in this operator basis, which looks as follows:

$$\varepsilon(\rho) = \sum_{m,n=0}^{d^2-1} \chi_{m,n} E_m \rho E_n^\dagger, \tag{2.14}$$

where is $d = 2^n$ is the dimension of the Hilbert space of the state ρ, χ is a $d^2 \times d^2$ process matrix of the quantum channel ε and E_i is an orthogonal basis in which the process is described, for which we use the Pauli basis in this work: $\{\mathbb{1}, X, Y, Z\}$. The χ process matrix, therefore, describes the transformation of an arbitrary quantum state caused by the quantum channel in an operator-sum representation.

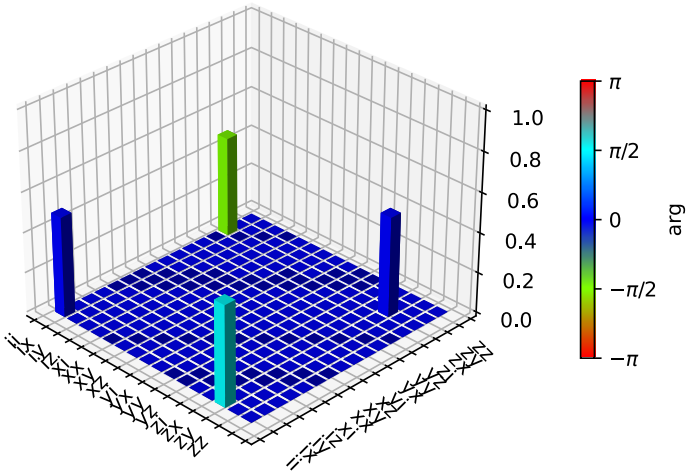

Figure 2.5: **Visualization of a process matrix for the conditional-$\frac{\pi}{2}$ rotation around x.** A quantum channel of an unitary process can be decomposed in the Pauli operator basis, in which the χ process matrix a complex-valued matrix that describes the contributions of the operator components to the process, therefore represents the process in the Pauli basis. The figures shows the components in the process matrix of conditional-$\frac{\pi}{2}$ rotation around x.

In order to preserve the CPTP constraints, χ must be positive-semidefinite, implying all non-negative real eigenvalues and Hermicity in order to preserve CP. TP is satisfied when:

$$\sum_{m,n} \chi_{m,n} B_n^\dagger B_m = \mathbb{1}. \tag{2.15}$$

We obtain the object χ for a simulated DDRF-gate using the QuTip software package in Python [12]. An overview of how χ is calculated with the software package is given in App. A.7. The fidelity of a gate F_p can then be obtained by finding the overlap of the generated χ from the DDRF gate with the process matrix of desired operation χ_{ideal}: $F_p = \text{tr}[\chi\chi_{\text{ideal}}]$. A visualization of the process matrix for a conditional $\pi/2$ rotation around x is shown in Fig. 2.5, which shows operator product that contribute to the process.

2.4.2 Error channels

Imperfections in the process can be represented by an error channel which models the underlying error process. If a gate is perfect, it should implement a unitary transformation and the process matrix matches the ideal. In reality, there is an effect of decoherence influencing the gate. Therefore to get a realistic estimate of the performance of a gate, we should characterize the error and then a realistic implementation of the gate can then be approximated, as a first order effect. In this work, we consider two types of error channels.

Dephasing channel

Dephasing is a gradual decrease of the phase information of a qubit, therefore the qubit looses its coherence. This can be modelled by a dephasing channel, where with a probability p the qubit flips its phase:

$$\varepsilon(\rho) = (1-p)\rho + pZ\rho Z. \tag{2.16}$$

Thus when the probability of a phase flip is 0.5, the qubit completely dephases.

This channel can be represented by a process matrix, where the non-zero elements are $\chi_{I,I} = 1-p$ and $\chi_{X,X} = p$.

Depolarizing channel

The effect of depolarization on a qubit is a loss of any information about the qubit. This can be modelled with a depolarizing channel, where the X, Y, Z Pauli operators are applied to the state with equal probability:

$$\varepsilon(\rho) = (1-p)\rho + \frac{p}{3}\big(X\rho X + Y\rho Y + Z\rho Z\big). \tag{2.17}$$

This channel can also be represented by a process matrix, where the non-zero elements are described by: $\chi_{1,1} = 1-p$ and $\chi_{X,X} = \chi_{Y,Y} = \chi_{Z,Z} = \frac{p}{3}$.

Chapter 3

DDRF spectroscopy and global window suppression

In this Chapter, we describe the characterization of the nuclear spins in the NV environment and develop new insight in DDRF. First, we explain the experiment to characterize the nuclear spins in the NV environment, a DDRF spectroscopy measurement. This allows us to estimate the hyperfine coupling of the nuclear spins. Moreover, the results of this experiment also reveal other interesting properties, such as a difference in driving efficiency of DDRF as a function of frequency, as already observed in Ref. [7]. We try to give an intuitive explanation in the form of an approximate suppression function, the so-called global window suppression. This suppression function is essential to understand the driving of the DDRF gate and eventually to design the gate for the desired operation to the system.

In Sec. 3.1, we explain the characterization of the nuclear spins using DDRF spectroscopy. Next, in Sec. 3.2, we introduce the global window suppression function.

3.1 DDRF spectroscopy

An approach to identify and characterize the nuclear spins surrounding the NV center is to apply a spectroscopy measurement with DDRF, where a range of DDRF gates with varying RF frequencies is applied to the NV. The sequence is shown in the inset of Fig. 3.1. We assume that all the nuclear spins are in a mixed-state (since $k_b T \gg \hbar\gamma B_z$), which can be written as $\rho_m = I/2 = (|+\rangle\langle+| + |-\rangle\langle-|)/2$. A first $\pi/2$-pulse brings the electron spin in a superposition state, if the RF frequency is on resonance with a nuclear spin during $m_s = -1$, a constructive buildup of rotations during the sequence happens from the matching of the RF phase with the spin phase. This generates a conditional evolution as shown in Eq. 2.13, and will decohere the electron spin as the nuclear spin is in a mixed-state. A second $\pi/2$-pulse applied to the electron spin projects the electron spin back onto the computational basis, allowing the signal detected. Fig. 3.1 shows this signal as a function of ω.

We can characterize the nuclear spins by associating the dips with a nuclear spin. During $m_s = -1$, the resonance frequency of a nuclear spin is approximated by $\omega_1 = \sqrt{(\omega_L - A_\parallel)^2 + A_\perp^2}$, and depends to first order on the parallel hyperfine component $A_\parallel$ of the spin. Therefore the position of a dip in the spectroscopy measurement can be related to the $A_\parallel$ of a nuclear spin, allowing the characterisation of the individual nuclear spins in the environment. A simulation of the DDRF spectroscopy measurement with the obtained hyperfine components shows a match with the experimental data in Fig. 3.1, verifying the nuclear spins. The effect of $A_\perp$ is a tilt of the quantization axis of the nuclear spin and a small shift in the resonance frequency during $m_s = -1$, introducing extra terms in the DDRF Hamiltonian 2.10 [7]. However, this effect is very small for the order of magnitude for the magnetic field that we are using, thus not forming a limiting factor [7]. Consequently, we obtain a list of 16 nuclear spins with their parallel hyperfine components (Tab. A.1).

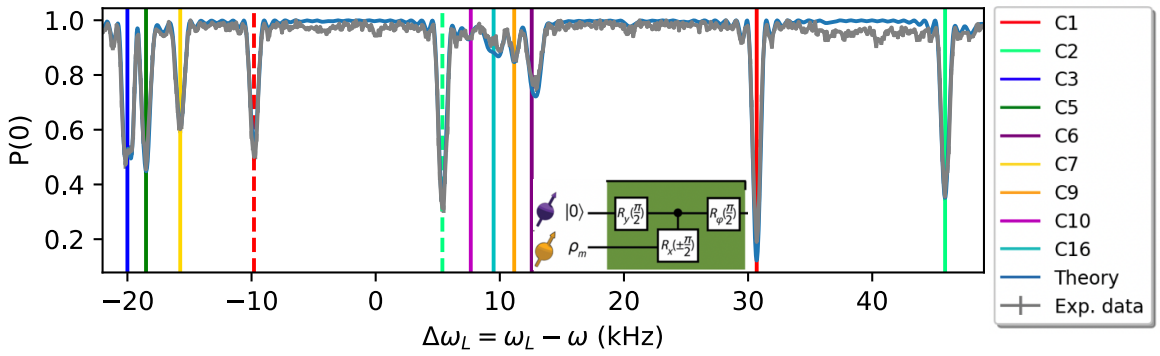

Figure 3.1: **DDRF spectroscopy.** The grey line shows the experimental result of the spectroscopy experiment shown in the inset, where a DDRF gate is applied at different RF frequencies. When the gate is on-resonance with the frequency of a spin during $m_s = -1$, constructive buildup of small rotations happens as the RF phase matches with the evolution of the spin during the sequence, therefore generating a conditional rotation. Hence the electron spin losses coherence due to the nuclear spin being in a mixed-state, which is signalled by a dip in the probability to read-out the electron in $m_s = 0$ at the end of the sequence. The blue line shows the result of a simulation of the experiment with a set of hyperfine parameters in A.1. Because of the overlap with the experimental data, we associate to the dips with nuclear spins, where the solid lines show the resonance frequencies during $m_s = -1$. The dashed lines are attributed to the driving of a nuclear spin at its harmonic. For clarity we show only a subset of the carbons.

3.1.1 Harmonics of nuclear spin

The fundamental principle for DDRF to coherently drive a nuclear spin is the constructive buildup of small rotations of the nuclear spin generated by the RF pulses during the periods in which the RF pulse is on-resonance (i.e. $m_s = -1$). To ensure this, the RF phases are updated to account for the accumulated phases of the nuclear spins during the off-resonant periods of the RF field (i.e. during $m_s = 0$). To illustrate this, consider an DDRF block ($\tau - \pi - 2\tau - \pi - \tau$) and the RF frequency set on-resonance with a nuclear spin. When the electron is in $m_s = -1$, the RF pulse slightly rotates the nuclear spin. After the π-pulse the electron is in $m_s = 0$, the RF-field is off-resonant, and the nuclear spin accumulates a phase of $\phi(\tau) = 2(\omega_L - \omega_1)\tau$. To be able to fully drive the nuclear spin during the next on-resonant period, the RF phase should match with the accumulated phase of the nuclear spin, hence updated with $2(\omega_L - \omega_1)\tau$. This principle allows us to drive the nuclear spin and pick up the signal at the resonance of the spin in Fig. 3.1.

The DDRF-spectroscopy measurements, however, also reveal other dips that are associated with nuclear spins, as marked by the dashed line in Fig. 3.1. These dips appear to be deep (indicating a strong interaction) close to the Larmor frequency and shift depending on τ, as can also be seen in Fig. A.2. This can be explained by closely examining the DDRF Hamiltonian in Eq. 2.10. Considering a specific nuclear spin frequency far detuned from the Larmor frequency ω_L during $m_s = -1$. Then if the RF frequency ω is set close to ω_L, the spin can not be driven as $\Omega \ll (\omega_1 - \omega)$, and therefore accumulates a phase $\phi_\tau(\omega) = (\omega_1 - \omega)\tau$ during $m_s = -1$. Moreover, during $m_s = 0$, the approximation $\Omega \ll (\omega_L - \omega)$ is not valid, therefore the spin is driven with the RF field. If in the special case the phase that is accumulated by the spin during $m_s = -1$ is a multiple of 2π, then the phase of the RF-pulse matches the phase of the nuclear spin during the next $m_s = 0$ block, and a a constructive build-up of rotations happens. This leads to additional driving resonances of a nuclear spin, which we call the harmonics, and show up at:

$$\omega_m = \omega_1 + \frac{\pi m}{\tau}, \tag{3.1}$$

for even integer m. Moreover, the cases of odd m correspond to a phase shift of multiples of π during the the off-resonant $m_s = -1$ periods, hence compensating the relative π phase in Eq. 2.12 required to generate a conditional rotation. The resulting evolution is therefore an unconditional rotation of the nuclear spin, and therefore not observed in the RF spectrum.

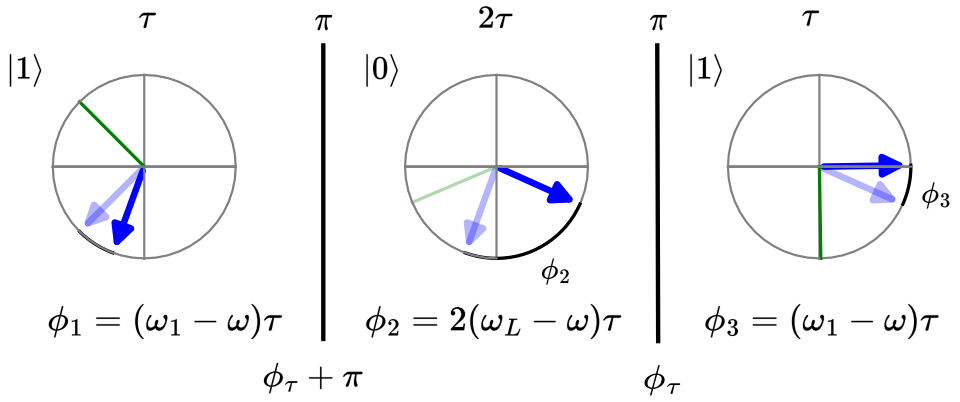

Figure 3.2: **Visualization of phase-matching during a single $(\tau - \pi - 2\tau - \pi - \tau)$ block.** (Shaded) green line represents the RF field (off)resonant with the nuclear spin resonance. (Shaded) blue represents the (initial) final phase of the nuclear spin during the period of τ. The RF frequency is set to the spin frequency during $m_s = -1$. The RF phase is updated with $\omega_\tau = (\omega_L + \omega_1 - 2\omega)\tau$ after each period, where the odd number of pulses have a relative π phase to ensure a conditional rotation, see Eq. 2.12. The total updated phase of the RF matches with the total accumulated phase of the nuclear spin, such that the situation after completion of the block is equal to the start.

3.2 Global window

Another observation of the DDRF-spectroscopy measurements is that not all the interactions are equally efficient, reflected by the depth of the dips shown in Fig. 3.1. As the total driving time (set by N and τ) is constant for each RF frequency, a suppression on the Rabi frequency should result in the varying strengths of the conditional rotation. This efficiency seems to depend on the detuning from both ω_L and ω_1.

In this Section, we elaborate on this effect and try to give an intuitive explanation using a suppression of the efficiency of the DDRF gates, which we call the global-window suppression. This gives a good first approximation of the effect, however, further research should be investigated to obtain an exact derivation. Understanding the driving efficiency of a DDRF-gate is an important requirement to create and optimize the desired operations in Ch. 4.

3.2.1 Phase-track driving

The way that the phases of the RF-pulses are updated play an important role in the total evolution of the nuclear spin during DDRF, as discussed before. In an attempt to visualize the efficiency of the DDRF gates at different RF frequencies, we start by observing that the phase-matching requirement can be generalized to any RF frequency, making the suppression become visible. To illustrate this, consider the RF frequency set to an arbitrary frequency ω, the total phase that a specific nuclear spin covers during a $(\tau - \pi - \tau)$ block can be seen from the DDRF Hamiltonian in Eq. 2.8:

$$\phi_\tau(\omega) = (\omega_L + \omega_1 - 2\omega)\tau. \tag{3.2}$$

Updating the RF-phase with $\phi_\tau(\omega)$ tracks the nuclear spin phase and ensures that the RF pulse matches the nuclear spin phase, which is illustrated in Fig 3.2. Ultimately, the total evolution will then depend on the ability of the RF field to rotate the nuclear spin conditionally at RF frequency ω. Fig. 3.3 shows the result of phase-track driving of a nuclear spin, where the RF phases are updated according to Eq. 3.2.

This leads to the observations that 1) the RF field has driving components at a wide range of RF frequencies which makes it possible to drive at all these frequencies, and 2) in some regions the

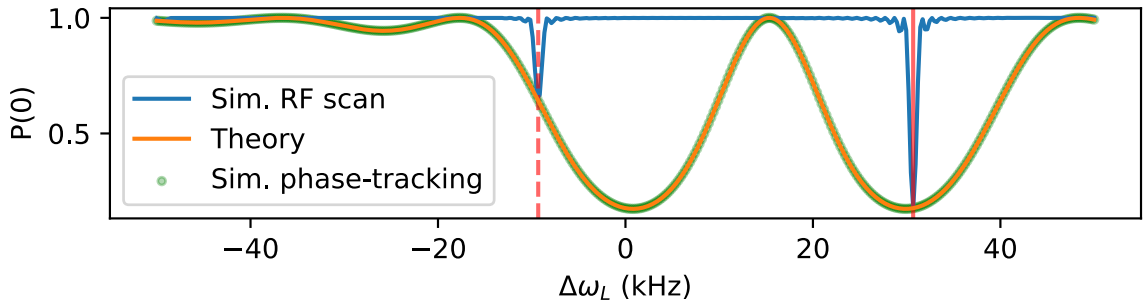

Figure 3.3: **Phase-track driving of C1.** Result of applying the spectroscopy measurement shown in the inset of Fig. 3.1 with normal RF phase-update according to the frequency in $m_s = -1$ (blue), and with RF phase updates in Eq. 3.2 (green) for C1. Orange line is the theoretical result from the global window function in Eq. 3.4, where the signal is calculated with $P(0) = \frac{1}{2}(1 - \cos(\phi))$ and ϕ is the conditional phase accumulated by the electron spin starting in $|+\rangle$ and equals the driving angle of the nuclear spin in Eq. 3.3. The gate is applied with $N = 40$, $\tau = 25$ μs and $\Omega = 200$ Hz. We conclude that each nuclear spin has its own global window, describing the strength of the driving at different frequencies when using the correct phase-updates. It therefore explains the strength of the dips in the DDRF spectroscopy measurement in Fig. 3.1, where the harmonic is shown to be a phase-matching condition (dashed red line).

ability to drive conditionally is suppressed. We call this suppression the global window suppression and it appears to depend on the relative positions of the two resonances and τ. Exactly in between the $m_s = 0$ and $m_s = -1$ resonance, there is a complete suppression, making it impossible to drive the spin conditionally. We recall that the conditionality of the driving is reflected by the angle θ in the total evolution operator for DDRF in Eq. 2.13. Before any further proof, we introduce a suppression to this angle $R_{\text{global}}(\Delta\omega_L, \Delta\omega_1, \tau)$, resulting in:

$$\theta = 2\pi\Omega N\tau R_{\text{global}}(\Delta\omega_L, \Delta\omega_1, \tau), \tag{3.3}$$

with

$$R_{\text{global}}(\Delta\omega_L, \Delta\omega_1, \tau) = \text{sinc}(2\Delta\omega_1\tau) - \text{sinc}(2\Delta\omega_L\tau), \tag{3.4}$$

where Ω is the Rabi frequency set by the amplitude of the RF-pulses, R_{global} is the suppression and $\Delta\omega_L = \omega_L - \omega$ and $\Delta\omega_1 = \omega_1 - \omega$ are the detunings from the ω_L and ω_1, respectively. Fig. 3.3 shows the signal of the analytical result from Eq. 3.4, and matches with the simulation. Conclusively, we introduced a suppression function for the driving ability of the DDRF gate in Eq. 3.4 without further derivation. As already explained this suppression function is an approximation and in the next Section we try to give a motivation for it.

3.2.2 Motivation for the global window

We start by computing the unitary evolution operators for a single RF pulse during $m_s = 0$ and $m_s = -1$, which gives the spin response of both resonances for specific DDRF parameters as a function of RF frequency. Consider the DDRF Hamiltonian in the rotating wave approximation in Eq. 2.10, which we restate for clarity:

$$H = |0\rangle\langle 0| \otimes \Delta\omega_L\sigma_z + |1\rangle\langle 1| \otimes \Delta\omega_1\sigma_z + \mathbb{1} \otimes \Omega\sigma_x, \tag{3.5}$$

where the first and last component of the tensor product acts on the electron and nuclear spin, respectively. The unitary evolution operator during a single RF pulse of time τ and the electron spin in a superposition state, takes the form:

$$U = |0\rangle\langle 0| \otimes U_0 + |1\rangle\langle 1| \otimes U_1, \tag{3.6}$$

with

$$U_0 = e^{-i\tau(\Delta\omega_L\sigma_z + \Omega\sigma_x)}, \tag{3.7}$$

$$U_1 = e^{-i\tau(\Delta\omega_1\sigma_z + \Omega\sigma_x)}. \tag{3.8}$$

Let us first consider U_0 in Eq. 3.10. This can be rewritten in the following way:

$$U_0 = e^{-i\phi\hat{n}\cdot\vec{\sigma}}, \tag{3.9}$$

where we define the unit vector $\hat{n} = \frac{\Delta\omega_L\hat{z}+\Omega\hat{x}}{\sqrt{\Delta\omega_L^2+\Omega^2}}$, the rotation angle $\phi = \sqrt{\Delta\omega_L^2+\Omega^2}\tau$ where $\sqrt{\Delta\omega_L^2+\Omega^2}\tau$ is the generalized frequency of the rotation around the unit vector and $\vec{\sigma} = (\sigma_x, \sigma_y, \sigma_z)$. By making use of the following Lemma:

Lemma 1 *Let $\hat{n}$ be an unit vector in $\mathbb{R}^3$ and let $S = e^{-i\phi\hat{n}\cdot\vec{\sigma}}$ be a rotation on the state space of a qubit. Then $S = \cos\phi\mathbb{1} - i(\hat{n}\sin\phi)\cdot\vec{\sigma}$.*

This gives:

$$U_0 = \cos\left(\sqrt{\Delta\omega_L^2+\Omega^2}\tau\right)\mathbb{1} - i2\pi\Omega\tau\,\mathrm{sinc}\left(2\sqrt{\Delta\omega_L^2+\Omega^2}\tau\right)\sigma_x - i2\pi\Delta\omega_L\tau\,\mathrm{sinc}\left(2\sqrt{\Delta\omega_L^2+\Omega^2}\tau\right)\sigma_z, \tag{3.10}$$

where we have used the definition $\mathrm{sinc}(x) = \frac{\sin(\pi x)}{\pi x}$. Similarly for the $m_s = -1$ case we obtain:

$$U_1 = \cos\left(\sqrt{\Delta\omega_1^2+\Omega^2}\tau\right)\mathbb{1} - i2\pi\Omega\tau\,\mathrm{sinc}\left(2\sqrt{\Delta\omega_1^2+\Omega^2}\tau\right)\sigma_x - i2\pi\Delta\omega_1\tau\,\mathrm{sinc}\left(2\sqrt{\Delta\omega_1^2+\Omega^2}\tau\right)\sigma_z. \tag{3.11}$$

To gain an intuitive picture for the global window suppression, we make the observation that both operators contain a driving term (i.e. a rotation around $\hat{x}$) that is set by the rotation angle $2\pi\Omega\tau$ and a suppression to this angle in the form of a sinc function, which is a function of τ, Ω and the detuning of the RF frequency to the resonances. Fig. 3.4A shows the spin response/driving components in Eq. 3.10 and Eq. 3.11 of both resonances for a nuclear spin as a function of RF frequency and varying τ. For $\omega = \omega_1$, we see that for some τ the spin response overlaps with the other resonance ω_L, and similarly for $\omega = \omega_L$. Hence, we conclude that for certain values of τ, the RF pulse is not selective on ω_1, and driving during $m_s = 0$ is also possible.

To understand how this influences the DDRF gate, we recall that the evolution of the nuclear spin during a gate depends on the electron spin initially in $m_s = 0$ or $m_s = -1$, such that during the sequence the rotations of the nuclear spin built up towards $|+\rangle$ or $|-\rangle$, respectively. This is set by the relative π phase difference between the odd (resonant during $m_s = 0$) and even (resonant during $m_s = -1$) RF pulses during the sequence, ensuring anti-parallel rotation axes between both cases. This results, in combination with the overlap of the RF pulse with both resonances, that in the case the electron is in $m_s = 0$, the nuclear spin rotates with an angle set by the driving term in Eq. 3.10 in the opposite direction as during the on-resonance period $m_s = -1$, leading to a sequential rotation reduction and accumulation. As a consequence, the net rotation after completion of the sequence is smaller than the desired $\pi/2$ for a maximally-entangling gate, hence resulting in a suppression to the intended operation.

This suppression can be approximated by the difference in the rotation angles between the resonances in $m_s = 0$ and $m_s = -1$ caused by the RF pulse, resulting in:

$$\theta = 2\pi\Omega N\tau\big(\mathrm{sinc}(2\Delta\omega_1\tau) - \mathrm{sinc}(2\Delta\omega_L\tau)\big), \tag{3.12}$$

where we can recognize the suppression term in Eq. 3.4 and $\mathrm{sinc}\left(2\sqrt{\Delta\omega_1^2+\Omega^2}\tau\right) \approx \mathrm{sinc}(2\Delta\omega_1\tau)$. The total conditional evolution of the gate is determined by the net rotation, which we can approximate using the suppression function. Fig. 3.2 shows that this also allows us to estimate the strength of the interactions with the harmonic of a nuclear spin observed in the RF spectra, which depends on the detuning from the resonances during $m_s = 0$ and $m_s = -1$. Altogether, this approximate function enables us to estimate the driving efficiency of a nuclear spin for specific DDRF parameters, and we obtained this function using the idea that a loss of selectivity of the RF pulse results in a suppression of the ability to drive conditional with a DDRF gate.

Moreover, there are also values of τ in which the rotation during $m_s = 0$ is negative, resulting in an extra rotation in the direction of the $m_s = -1$ rotation, and hence generating an enhancement of the conditional driving. Fig. 3.2B. shows the difference in the rotation angle as a function of RF frequency. A negative difference accounts for the case of a conditional rotation in the opposite direction, i.e. $\mathrm{CR}_x(\pm\theta)$ becomes in $\mathrm{CR}_x(\mp\theta)$. By applying the idea of phase-track driving, where the phase is updated according to Eq. 3.2, this could lead to interesting possibilities of optimizing the RF frequency to increase the efficiency of the conditional driving of a gate.

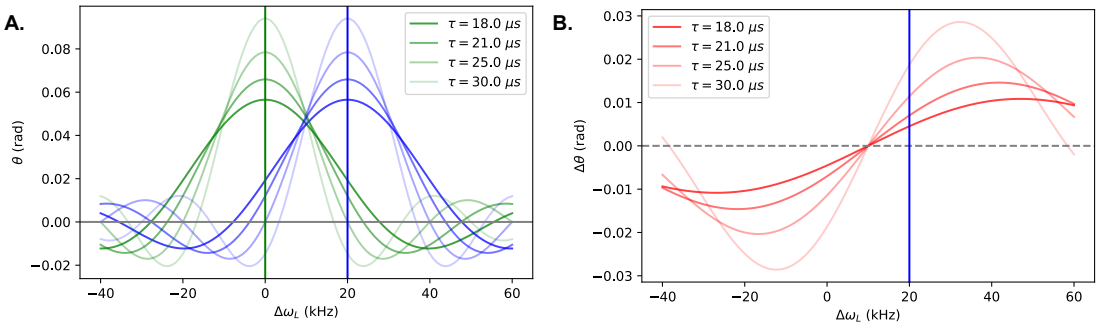

Figure 3.4: **Spin-response for $m_s = 0$ and $m_s = -1$ resonance. A.** Green (blue) lines show the spin response for resonance of the spin during $m_s = 0$ ($m_s = -1$) in Eq. 3.10 and Eq. 3.11, for a nuclear spin that is 20 kHz detuned from ω_L during $m_s = -1$. For certain values of τ, the spin-responses overlap, reducing the selectivity. **B.** The difference in the rotation angle between $m_s = 0$ and $m_s = -1$, reflecting the ability of the gate to do a conditional gate. By applying phase-track driving, where driving at a frequency ω is possible using updating the phase with Eq. 3.2, this could lead to an enhancement of the conditional driving efficiency of a gate.

3.2.3 Approximate result of the global window function

So far, we have only given a qualitative argument for the global window function in Eq. 3.4. As it is currently not possible to derive an exact result for this effect from the unitary evolution operator in Eq. 3.6, we provide in this section a quantitative argument on the ability of the global window suppression to approximate the observed behaviour of the DDRF gate. To test the approximate behaviour of the global window suppression function, we compare the function with simulations on a large parameter space by analyzing the residuals, where we are especially interested in our regime of $\theta \approx \frac{\pi}{2}$.

Fig. 3.5 shows the result for the behaviour of the residues for different parameter spaces. For a correct comparison, we fix the product $2\pi\Omega N\tau$, ranging from 0 to 6π. This shows that for the three parameters, the residues are below 10^{-4} in our regime, but increase up to 10^{-2} for large products of $2\pi\Omega N\tau$. Hence, we conclude that for the three parameters, the global window suppression is at least a valid approximation in the regime we are working in.

3.3 Conclusion

In this Chapter, we have discussed the signals coming from DDRF in more detail. We have used this to characterize 16 ^{13}C atoms possessing a nuclear spin that couples strongly to the NV, and thus can be used as possible qubit resources. Next, we have addressed the driving efficiency differences of the spins observed in the RF spectrum and gave a possible qualitative argument using the global window function, describing a suppression of the ability to drive the spin conditionally due to a sequential rotation reduction and accumulation generated by the RF pulses during the sequence.

Ultimately, the suppression function will allow us to understand the design of the gates in the next chapter.

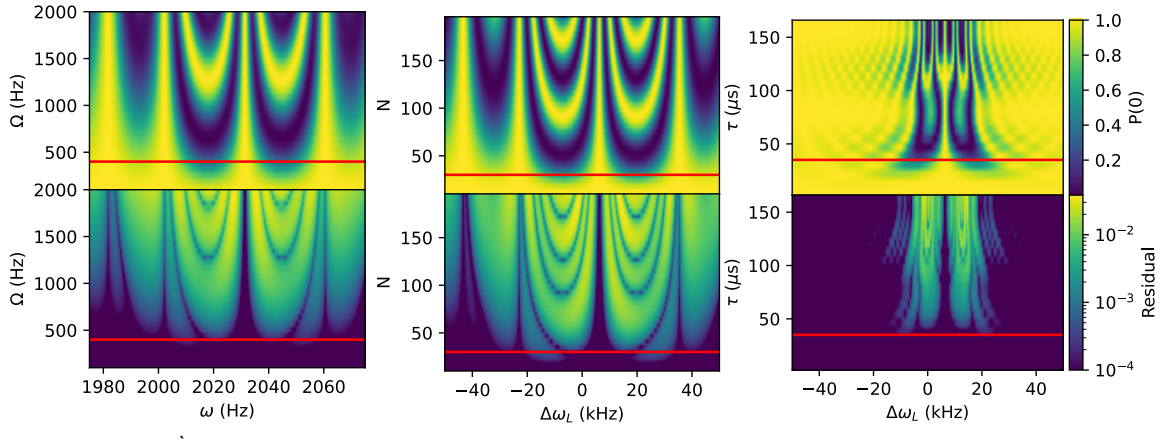

Figure 3.5: **Comparison of the global window suppression with the simulations.** We compare the global window suppression with the simulations by subtracting both analytical result from the simulations, and investigate their residues, which reflects how well the analytical result approximates the behaviour. We do this for a large parameters space, where we investigate the dependence of the approximation on the DDRF parameters. The top panel is the electron-read out signal for the given parameters. The product $2\pi\Omega N\tau$ ranges from 0 to 6π for correct comparison. The red line indicates the regime $\theta \approx \frac{\pi}{2}$. We conclude that the global window function approximates the simulations well in this regime.

Chapter 4

Optimization of the DDRF gates

In this Chapter, we focus on the design and optimization of the DDRF gates. To design gates that generate the desired operation on the system amounts to finding the right combination of parameters for the gate. Hence, we need the global window suppression function from Ch. 3 to obtain the suppression for each choice of parameters. Secondly, we are interested in optimizing the DDRF gates to obtain high fidelity gates. For this, we investigate the effect of three types of decoherent noise sources on the DDRF gates to simulate realistic gates. Moreover, to eventually characterize and verify the fidelity of the gates, we use the process matrix formalism introduced in Sec. 2.4, from which we can obtain the gate fidelity for a particular gate design. The intended operation is a two-qubit maximally entangling gate between the electron and nuclear spin. We run this optimization procedure for the whole nuclear spin register found in Ch. 3, which eventually will allow us to simulate the protocols in the next Chapter.

In Sec. 4.1, we describe the space of parameters for the DDRF gates set by the global window suppression and bounded to certain constraints to be physically realizable. This yields a set of parameters for each nuclear spin in the register that generates the desired operation. Then in Sec. 4.2, we look into the effect of decoherent noise sources on the set of gates for each nuclear spin. This eventually allows us to obtain a measure of the fidelity of a DDRF gate, helping to understand the parameter space, what are the limitations and what are the trade-offs for the desired operations, as will be discussed in Sec. 4.3.

4.1 Parameter space for DDRF-gates

To obtain the desired operations for the system, we carefully have to design the DDRF-gates. From now on, we drive DDRF on resonance with the frequency of a nuclear spin during $m_s = -1$ resonance frequency of a spin (i.e. $\omega = \omega_1$). Hence, the conditional evolution operator of DDRF in Eq. 2.13 depends on four parameters: the number of decoupling pulses N, the decoupling time τ, the Rabi frequency Ω (which is related to the amplitude of the applied RF-pulses) and the phase ϕ of the RF-pulses. The product of N and τ amounts to the total driving time, whereas the driving speed is set by Ω, and ϕ sets the rotation axis.

The global window suppresses the efficiency of the DDRF-gate, affecting the desired evolution. As shown in Ch. 3, this effect depends on τ and detuning from the Larmor frequency $\Delta\omega_L$. This suppression determines the conditionality of the gate, such that the angle of the conditional rotation operator in Eq. 2.13 is set by:

$$\theta = 2\pi N\Omega\tau R_{\text{global}}(\Delta\omega_L, \Delta\omega_1, \tau) = 2\pi N\Omega\tau\big(1 - \text{sinc}(2\pi\Delta\omega_L\tau)\big), \tag{4.1}$$

where $R_{\text{global}}(\Delta\omega_L, \Delta\omega_1, \tau)$ is the global window suppression with $\Delta\omega_1 = 0$. Consequently, a maximally-entangling gate is achieved by setting the parameters such that the Eq. 4.1 equals $\frac{\pi}{2}$, which creates a CNOT-gate up to single qubit gates. This set of parameters forms an effective space for DDRF gates.

In principle, the space of DDRF gates is infinite. To make sure that the gates are physically realizable we consider bounds on this space, and eventually conclude if these bounds include regions of high fidelity gates. First, the total allowed gate time is set to 3 ms. This is to minimize the overall sequence time when applying multiple gates to reducing natural dephasing of the spins. Secondly, to

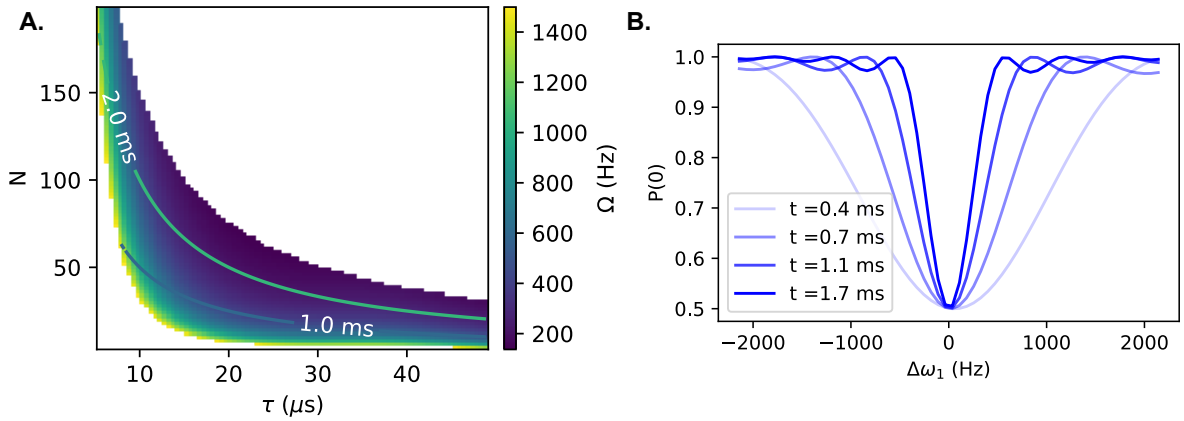

Figure 4.1: **DDRF parameters space on-resonance.** **A.** Visualization of the DDRF-parameterspace for maximally entangling gates. The isolines indicate the gate time ($2N\tau$). For each combination of N and τ, the Ω is optimized such that the parameters satisfy $2\pi N\Omega\tau R_{\text{global}} = \frac{\pi}{2}$. The maximal gate time is set to 2 ms, the maximal allowed Rabi frequency is set to 1500 Hz and the maximum inter-pulse time is set to 50 μs. **B.** Spin response for DDRF gates with different driving times. We conclude that long times increases the selectivity.

prevent heating of the sample when applying the RF pulses, the Rabi frequency is limited to 1500 Hz. Moreover, to decouple the electron spin from interactions with isolated nuclear spins and the spin-bath, τ is set to multiples of $\tau_L = \frac{1}{\omega_L}$ and limited to below $50\mu s$. Fig. 4.1 shows the gate space for a nuclear spin in the register, which is detuned by 30 kHz from the Larmor frequency during $m_s = -1$. For each combination of N and τ, Ω is set such that the DDRF gate generates a conditional-rotation. The maximum allowed gate time then determines the bound along the outer shell, whereas the global window suppression determines the behavior on the inside. At small τ, this last effect becomes more severe and thus limits the efficiency: either the Rabi frequency or the number of pulses needs to be increased. Since both these parameters are bounded, the possibilities for a set of allowed parameters become restricted.

4.2 Decoherent noise sources

Given a set of DDRF gates, we are interested in their performance when subject to decoherent noise sources. In this work, we investigate three types of noises: crosstalk, nuclear- and electron- spin dephasing caused by the presence of a spin-bath. Evaluating these effects for each gate will allow us to obtain the optimal gate for the considered noises.

4.2.1 Crosstalk

Crosstalk is considered as unwanted interactions between the nuclear spins generated by the DDRF-gate such that the resulting quantum state diverges from the desired state. If we want to apply a two-qubit gate to create entanglement between the electron and a nuclear spin, the DDRF gate should ideally perform an Identity operation on the bystander nuclear spins. Explicitly, we ignore the operations on the bystander nuclear spins that can either be easily compensated for, or that do not affect the desired quantum state. For example, a phase shift on a bystander nuclear spin can be compensated by a waiting gate and does not affect the state of the electron spin. Similarly, an unconditional rotation on a bystander spin does not affect the electron spin and is therefore not considered as crosstalk if that spin is not in the register. Hence, we consider crosstalk as all the operations on the bystander spins apart from unitary transformations that do an Identity operation up to an unconditional phase shift (and rotation) when the bystander spin is (not) part of the qubit register.

In principle, the crosstalk effect from a DDRF gate can be obtained by the construction of the

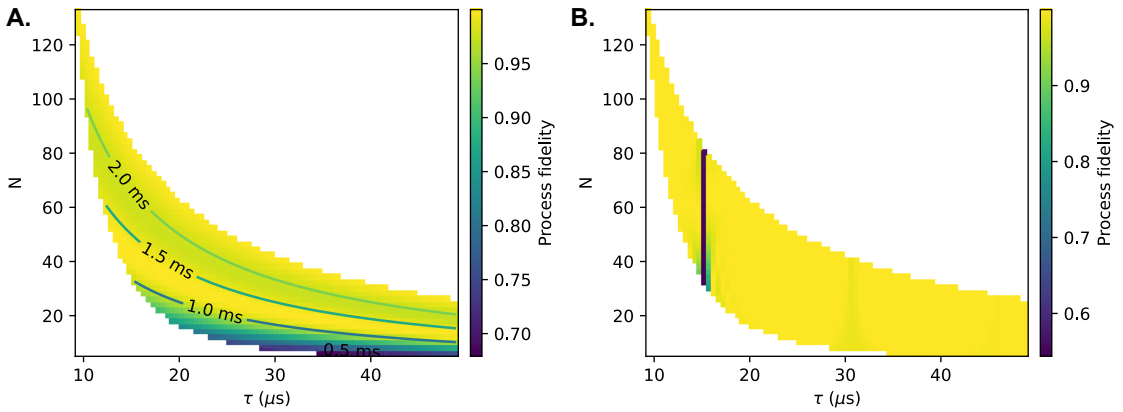

Figure 4.2: **Effect of crosstalk. A.** Crosstalk on C2 induced by DDRF-gates on C5. The high infidelity happening at low gate time indicates crosstalk coming from broad RF pulses overlapping with the resonances of the two nuclear spins.**B.** Crosstalk on C2 induced by DDRF-gates on C4. Localized peaks of infidelity are related to crosstalk coming from the overlap of the m order harmonic in Eq. A.12 of C4 with the driving frequency of the DDRF-gate, which depends on τ. Simulations are performed on the DelftBlue High Performance Cluster (DHPC) [14].

process matrix for the state of the full spin system, which ideally is:

$$\chi^{\mathbf{ideal}}(\omega, \Omega, N, \tau) = [\mathrm{CR}_x(\pm\frac{\pi}{2})] \otimes [\mathbb{1}]^{\otimes(N-1)}, \tag{4.2}$$

where the N is the total number of nuclear spins in the system, $CR_x\left(\frac{\pi}{2}\right)$ is a conditional-rotation between the electron and the target nuclear spin and $\mathbb{1}$ is the Identity operation up to local phases and rotations on the bystander nuclear spins. The construction of this process matrix becomes, however, impossible to calculate for a system with a large number of qubits. For a quantum state that lives in a Hilbert space of n qubits, the dimension of that space is $d = 2^n$. The software calculates the process matrix χ by constructing and inverting a matrix M with the size $d^4 \times d^4$, see App. A.7 [12]. This, therefore, becomes an almost impossible task for a large number of qubits [13].

However, we can work around this with the following observation. As the nuclear-nuclear interactions are typically in the order of a few Hz [10], these interactions are very small on the timescales of the gates, therefore not inducing crosstalk. Hence, the process matrix for a DDRF-gate in Eq. 4.2 will only have non-zero terms for the electron-nuclear interactions, and thus crosstalk is fully captured by each electron-nuclear interaction with the bystander nuclear spins. With this assumption, we simulate the crosstalk of a DDRF gate by considering the effect this gate has on the $(N-1)$ bystander nuclear spins in the node, which can be represented by $(N-1)$ separate two-qubit process matrices. Crosstalk is then reflected by an infidelity with respect to an Identity operation up to an unconditional phase (rotation) when the nuclear spin is (not) part of the qubit register. This results in a set of $(N-1)$ gate maps, as displayed in Fig. A.4. Fig. 4.2 shows two of these infidelity maps, where a decrease in process fidelity indicates crosstalk. Two interesting features can be seen from this. First, crosstalk can occur at specific values of τ. This is explained by an interaction with the harmonic of a bystander nuclear spin (Sec. 3), where the m-th order harmonic ω_m of a bystander spin matches with the RF frequency ω of the gate, therefore driving the spin. As discussed in Sec. 3.1.1, the position of the harmonic frequencies depend on τ and therefore the crosstalk shows up at specific values of τ. Note that this also captures unconditional rotations. The second effect results from a loss in selectivity of the RF pulses when two spins are spectrally-close, resulting in simultaneous driving of both spins. Broad RF-pulses happen at short pulses, therefore the effect of crosstalk is strong at gates with small sequence time. However, increasing the allowed maximum gate time results in more selective RF-pulses, therefore reducing this type of crosstalk.

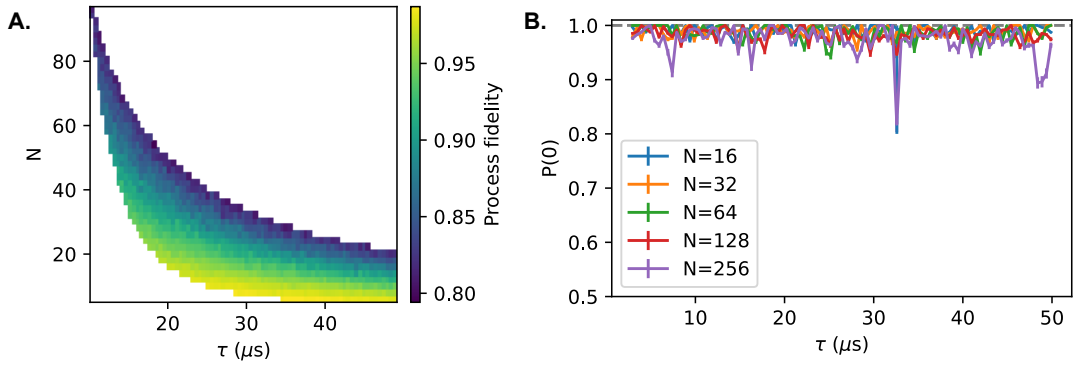

Figure 4.3: **Decoherent noise sources. A.** Effect of nuclear spin dephasing for all the gates in the parameter space where the effect of nuclear spin dephasing is calculated using Monte-Carlo methods and reflected by an process infidelity. The isolines reflect the gate time. **B.** Electron coherence data. Results of DD data from the experiment for different waiting time τ and N, showing the remaining electron coherence. No significant loss is witnessed throughout the whole space.

4.2.2 Nuclear spin dephasing due to the spin-bath

As a second source of decoherence, we consider the effect of the nuclear spin-bath on the performance of the DDRF gates. The spins in the spin-bath are very weakly coupled and precess at near ω_L frequency during $m_s = -1$, therefore flip-flop interactions between the nuclear spins in the spin-bath occur with a high probability. This results in a time-varying spin configuration of the spin-bath that induces a quasi-static fluctuation of the magnetic field felt by the nuclear spin and electron spin. These magnetic fluctuations follow a Gaussian distribution with a standard deviation of:

$$\sigma_B = \frac{2}{\sqrt{2} T_2^* \gamma_c}, \tag{4.3}$$

where T_2^* is the characteristic dephasing time for the nuclear spin. Assuming a typical T_2^* of 10 ms, this results in magnetic fluctuations of the order of 10 mG.

To simulate the effect of quasi-static magnetic fluctuations on the performance of the DDRF gates, we use Monte-Carlo methods. A single DDRF gate is simulated 300 times while varying the magnetic field with fluctuations drawn from a Gaussian distribution with the standard deviation in Eq. 4.3. The average process fidelity then reflects the effect of the nuclear spin dephasing. In principle, each nuclear spin has a different T_2^* time, which is measured from the decay of a free precession measurement (Ramsey) [15], but since these measurements were not finished, we assumed a T_2^* time of 10.8 ms for all the nuclear spins [15, 16]. Fig. 4.3A depicts the result of such a Monte-Carlo simulation for the whole gate space of a nuclear spin.

The infidelity introduced by the nuclear spin-bath scales with the sequence time of the gate, as shown in Fig. 4.3A. No clear distinction between the number of decoupling pulses N and the waiting time τ on the effect of nuclear spin dephasing is observed, concluding that the main objective for reducing the decoherence caused by the spin-bath is the limitation on gate time.

4.2.3 Electron coherence lifetime

Lastly, we want to learn about the ability of the DDRF gate to protect the electron coherence. As the gyromagnetic ratio of the electron is three orders of magnitude higher than for the carbon atom, the electron spin experiences significantly more dephasing due to the quasi-static fluctuations from the spin-bath. In addition, the electron spin also couples to individual strongly-coupled nuclear spins.

To protect the coherence of the electron spin, the DDRF-gate exploits dynamical decoupling (DD) sequences. In general, the electron spin can be decoupled from interactions with an oscillating magnetic field if the oscillation frequency is off-resonant to the interpulse frequency $1/(2\tau)$ of a DD sequence. Therefore the interpulse time τ is optimized to decouple the electron spin from unwanted interactions with individual spins and the spin-bath.

Ideally, τ should be kept short and set to multiples of $\tau_L = 1/(\omega_L)$. The first constraint is due to the quasi-static fluctuations of the magnetic field induced by the spin-bath. When τ is comparable to the magnetic fluctuations, this effect becomes apparent during both free precession times. Therefore the dephasing before and after the π-pulse are not the same, and thus will not echo out by the DD sequence. Furthermore, setting τ to multiples of τ_L protects the electron spin from interactions with strongly coupled nuclear spins, as during $m_s = -1$ no nuclear spin precesses with ω_L.

To optimize the DDRF gates for a long electron coherence lifetime, we experimentally verify the robustness of the DD parameters in the parameter space to sustain electron coherence. Fig. 4.3B shows the remaining electron coherence after a DD gate is applied with the respective N and τ, where dips in the electron coherence indicate unwanted interactions. We conclude from this data that specific values of τ reveal coupling and should thus be avoided. These could originate from experimental errors or coupling with pairs in the environment. Although this may unlock interesting opportunities, such as storing quantum information in a decoherence-free subspace [17], this requires further analysis of the nuclear spin environment, therefore out of scope for this project. Moreover, verifying the robustness with coupling to the weakly-coupled spin-bath, a decay envelope should be fitted to the overall decaying signal. Given the current data, it is not possible to fit a decay function, however, we can conclude no strong losses are visible up to $50\mu s$ in App. A.2. This confirms the limit on τ set in Sec. 4.1.

4.3 Estimation of the gate fidelity

The last step in optimizing the DDRF-gates is to obtain an estimate of the gate fidelty, allowing the characterization of regions with high fidelity gates within the parameter space. To summarize, in Sec. 4.1 we obtained the complete set of DDRF gates generating the desired operation for each nuclear spin in the sample. Subsequently, Sec. 4.2 examined the performance of the gates regarding the three types of noise sources. Here we develop a model to estimate the gate fidelity using an error process matrix.

For our approach, we model the two-qubit unitary process as a process that first performs a perfect unitary (i.e. a conditional rotation) and then an error channel, as illustrated in Fig. 4.4. This error map can be represented by an error process matrix χ^{err}. The total process of the DDRF-gate is then modelled as [18]:

$$\rho_{\text{out}} = \varepsilon_{\text{total}}(\rho_{\text{in}}) = \sum_{m,n} \chi^{\text{err}}_{m,n} E_m U_{\text{ideal}} \rho_{\text{in}} U^{\dagger}_{\text{ideal}} E^{\dagger}_n, \tag{4.4}$$

where U_{ideal} is a conditional $\pi/2$ rotation around x on the nuclear spin, $\rho_{\text{in}}(\rho_{\text{out}})$ is the initial (final) state and $E_{m,n}$ are operators in the Pauli basis in which the process is decomposed. In the ideal case, the error matrix χ^{err} corresponds to an Identity operation, therefore only having a non-zero element at the $(0,0)$ entry which corresponds to the II operator product. Any other non-zero term thus indicates imperfections in the process. This gives the advantage to obtain the fidelity of the gate directly from the error matrix:

$$F_p = \text{tr}\left[\chi^{\text{err}} \chi_{\mathbf{I}}\right] = \chi^{\text{err}}_{0,0}, \tag{4.5}$$

where $\chi_{\mathbf{I}}$ corresponds to the desired error matrix, i.e. Identity. Conclusively, the construction of the error matrix for a particular DDRF-gate gives access to the gate fidelity.

The total error matrix is built up from the separate error process matrices, resulting in:

$$\chi^{\text{err}} = \chi^{\text{err}}_{\text{crosstalk}} \chi^{\text{err}}_{\text{electron}} \chi^{\text{err}}_{\text{nuclear}}, \tag{4.6}$$

where $\chi^{\text{err}}_{\text{crosstalk}}$, $\chi^{\text{err}}_{\text{electron}}$ and $\chi^{\text{err}}_{\text{nuclear}}$ are the process matrices for the effect of crosstalk, electron coherence loss and nuclear spin dephasing, respectively. Hence, we need to obtain each seperate error matrix.

Error matrix for crosstalk

Considering a single DDRF-gate acting on the j-th nuclear spin, we want to estimate the error that this gate induces due to the effect of crosstalk. As discussed in Sec. 4.2.1, this effect is captured by the $(N-1)$ two-qubit process matrices between the electron and $(N-1)$ bystander nuclear spins, for which we calculated the process fidelity with respect to Identity. Hence, this reflects the amount of conditional rotation on a bystander nuclear spin that the DDRF-gate generates, resulting in a phase

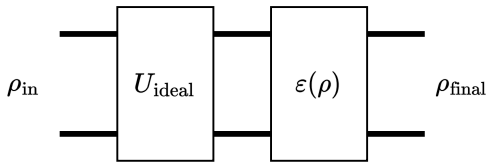

Figure 4.4: **Model for two-qubit gate.** The desired two-qubit gate operation U_{ideal}, which maps ρ_{in} to ρ_{final}, is modelled as first the ideal operation and then an error channel $\varepsilon(\rho)$, as described in Eq. 4.4. The error channel is then represented by an error matrix χ^{err}, that is constructed using the decoherent noise sources.

accumulated by the electron spin. For that reason, we model the effect of crosstalk by a dephasing channel on the electron spin, represented by a process matrix:

$$\chi^{\text{err}}_{\textbf{nuclear}} \begin{cases} \chi_{II,II} = 1 - p, \\ \chi_{ZZ,ZZ} = p, \end{cases} \tag{4.7}$$

where p is the error probability. To obtain a realistic model of the crosstalk effect, we need to relate this error probability to the outcomes of the crosstalk simulations.

To find a realistic representation for the error probability p, we make the following observation. Within the process matrix formalism, the process is described in an operator-sum representation, where the χ process matrix represents the contributions of the operators-products in the Pauli basis. For a conditional rotation, the operator-sum representation only contains contributions of non-identity operator products (i.e. $XX, XY, XZ...$) plus the II operator, as is visualized also in Fig. 2.5. Moreover, if the angle of the conditional rotation matches π, the conditional rotation transforms into an unconditional phase-flip, ZZ. From this, we learn that if we measure the process fidelity with respect to the Identity operation, which is determined by the overlap with the II contribution, this ranges from 1 (perfect Identity operation) to 0 (phase-flip). Conclusively, we model the error probability $p = 1 - F^I_j$, where F^I_j is the process fidelity with respect to Identity on the j-th nuclear spin due to a gate on the i-th nuclear spin.

Furthermore, capturing the crosstalk effect to the full system, we approximate this by sequentially applied dephasing channels:

$$\chi^{\text{err}}_{\text{ct},i} = \prod_{i \neq j}^{N-1} \chi^{\text{err}}_{\text{ct},j}, \tag{4.8}$$

where the crosstalk effect of a gate on the i-th nuclear spin is the product of $(N-1)$ dephasing channels.

Error matrix for the electron coherence loss

The error matrix for the loss of electron coherence during the gate is modeled by a dephasing channel on the electron spin. As described in Sec. 4.2.3, the objective is to decouple the electron from unwanted interactions with its environment by exploiting DD sequences. A measure that reflects the ability of the DD sequences to achieve this is the remaining electron coherence after a DD sequence, which is described by the probability $P(0)$ to measure the electron in $m_s = 0$. When $P(0) = 1$, the electron has perfectly decoupled and no dephasing occurred. In contrast, if $P(0) = 0$ the electron underwent an interaction with a single nuclear spin and the electron achieved a phase-flip, i.e. $\chi_{Z,Z}$. Moreover, if the $P(0) = 0.5$, the electron is coupled to the full spin-bath and the spin is completely dephased. $P(0)$, therefore, models the dephasing probability of the electron spin, and the error process matrix for the loss of electron coherence becomes:

$$\chi^{\text{err}}_{\text{electron}} = \begin{cases} \chi_{II,II} = 1 - p, \\ \chi_{ZZ,ZZ} = p, \end{cases} \tag{4.9}$$

with $p = 1 - P(0)$.

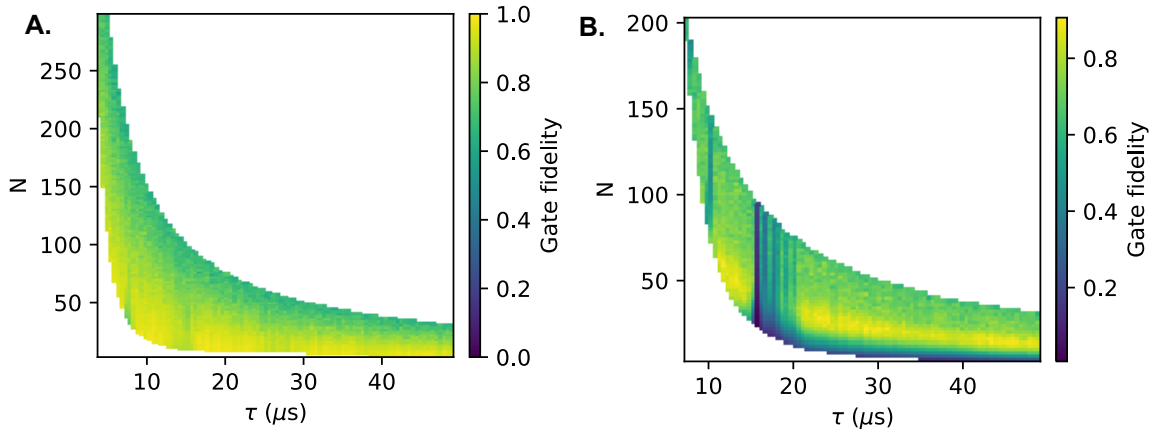

Figure 4.5: **Estimate of gate fidelity for C1 and C4.** Using the model in Eq. 4.4, we evaluated the gate fidelity for all the DDRF gates. For C1 (**A**), the effect of crosstalk is minimal, therefore allowing to drive very efficient. For C4 (**B**) the gates suffers from crosstalk, resulting in a balance between selectivity and efficiency. Eventually the region with highest fidelity gates are within the bound of maximum gate time.

Error matrix for nuclear spin dephasing

Lastly, the error channel from the effect of the nuclear spin dephasing caused by the spin-bath during a DDRF gate, is represented by a process matrix:

$$\chi^{\text{err}}_{\text{nuclear}} = \begin{cases} \chi_{II,II} = 1-p, \\ \chi_{ZZ,ZZ} = p, \end{cases} \tag{4.10}$$

with $p = 1 - F_{\text{CROT}}$, where F_{CROT} is the average process fidelity simulated using Monte-Carlo methods in Sec. 4.2.2, resulting in a complete dephasing of the spin when the fidelity goes to 0.5.

Although this approximates the effect to first order very well, we note an extra consideration introduced by the nature of the simulation and the complexity of the process matrix. First, we recall that the simulation applies a fluctuation of the magnetic field drawn from a Gaussian distribution in Eq. 4.3 while applying the gate with the DDRF parameters repeatedly, such that the average process fidelity reflects the effect of the dephasing. When a particular gate is selective, the effect of a large magnetic fluctuation on the evolution generated by the gate goes to an Identity operation, i.e. a process fidelity of 0.5 with the ideal process. Moreover, in the intermediate regime, the effect of a slight magnetic fluctuation is two-fold: the rotation angle decreases and the rotation axis shifts, introducing different infidelities. The first effect introduces an increasing contribution of the II in the process matrix whereas the second introduces contributions of ZY operators. Due to the complexity of the process matrix, the second effect allows slightly below 0.5 process fidelities, leading to slight imperfections in the modelling of the error probability.

For a complete description, we refer to the method described in Korotov et al. 2013 [18]. Constructing the average process matrix χ^{meas} during the Monte-Carlo simulation provides a complete description of the process in presence of a spin-bath. The error matrix can be calculated from:

$$\chi^{\text{err}} = V\chi^{\text{meas}}V^{\dagger}, \quad \text{where} \quad V_{mn} = \text{tr}\left[E_m^{\dagger}E_n\chi^{\text{ideal}\dagger}\right]/d, \tag{4.11}$$

with d the dimension of the process matrix, i.e. 16. Modelling the effect of nuclear spin dephasing using the average process matrix χ^{meas} gives a rigorous model to obtain the process fidelity, and will be interesting for future application to optimize the DDRF gates, however due to time limit we were not able to incorporate this, and since it behaviour infidelities arising from this object are very similar as the method we employed.

Ultimately, given each separate error process matrices, we are able to estimate the gate fidelity using 4.5. Fig. 4.5 shows the gate fidelity for the parameters space of two nuclear spins.

4.4 Conclusion

In this Chapter, we investigated the optimzation of DDRF gates to create gates that avoid crosstalk and protect the coherence of the system, needed for the realization of large qubit registers. We studied the complex space of DDRF gates generating the desired operation. Next, we investigated the effect of the dominant noise sources on this parameter space. We clearly saw a balance between selective and efficient gates suffering from either dephasing or crosstalk. To find the optimal gates for each spin, we have developed a model that estimates the gate fidelity using error process matrices. This revealed that the bounds we set for the parameter space include the region high-fidelity gates for all the spins.

Chapter 5

Performance of the qubit-register

In this Chapter, we investigate the performance of the qubit register. We do this by simulating protocols that generate Greenberger-Horne-Zeilinger (GHZ) states with an increasing number of qubits and evaluate the GHZ-state fidelity as a function of the number of qubits, reflecting the performance of the qubit-register. In Ch. 4, we optimized the DDRF gates for the nuclear spin register found in Ch. 3. Now we apply these gates within the protocols to create large GHZ-states. In particular, we focus on three types of setups. The first scenario is a single-node register. Next, we investigate the performance of network registers, considering two- and three-node networks. This follows the experimental demonstrations in Ref. [8], where the first multi-node entangled network of NV centers has been created. The potential to scale the qubit register over multiple nodes will allow future demonstrations of distributed quantum computing.

In Sec. 5.1, we describe the modelling of the two-qubit gates during the protocols. Next, we present the single node and the network protocols and discuss the resulting performances in Sec. 5.2.

5.1 Simulating the gates during the protocol

As a protocol consists of single- and two-qubit gates, here we describe how to model these gates. First of all, we assume perfect single-qubit gates on the electron. The two-qubit gates are modelled in the same way as described in Eq. 4.4 of Sec. 4.3, where the gate is modelled as first an ideal operation and after that an error channel. The error channel can be represented by a process matrix that is constructed using input from the decoherent noise sources, as shown in Sec. 4.3. Considering a two-qubit gate on the i-th nuclear spin, the effect of crosstalk is modelled by a dephasing channel on the electron spin that is represented by the error process matrix $\chi^{\text{err}}_{\text{ct},i}$ in Eq. 4.8. The nuclear spin dephasing is modelled by a two-qubit dephasing channel represented by the error process matrix $\chi^{\text{err}}_{\text{nuclear},i}$ in Eq. 4.10. Lastly, the effect of electron coherence loss is modelled by a dephasing channel on the electron spin as represented by the error process matrix $\chi^{\text{err}}_{\text{electron},i}$ in Eq. 4.9. This ensures that the gate is modelled realistically, giving a realistic interpretation to the protocol simulations.

T_2^* effect of the nuclear spin

In addition, quasi-static fluctuations of the spin-bath dephase the nuclear spin when it is set in a superposition state, hence this effect is also implemented in the protocol simulations. A dephasing channel on the nuclear spin does this, where after a gate of time t, the set of qubits already in a superposition state are subject to this channel. We thus need to model the dephasing probability p. Assuming that the quasi-static fluctuations of the spin-bath follow a Gaussian distribution, the T_2^* decay of the Ramsey fringes during a time t follow $\frac{1}{2} + \frac{1}{2}\exp\big(-\frac{1}{2}(\frac{t}{T_2^*})^2\big)$, where T_2^* is the characteristic decay time. We were unable to measure the decay times for each individual nuclear spin and therefore we assume a typical time of $10.8ms$ [16]. The amplitude of the Ramsey signal then decays due the T_2^* effect and ranges from 1 (no dephasing) to 0.5 (completely dephased). Hence, the error probability p of the dephasing channel in Eq. 2.16 is modelled by $\frac{1}{2} - \frac{1}{2}\exp\big(-\frac{1}{2}(\frac{t}{T_2^*})^2\big)$.

5.2 Protocols

A protocol for the creation and detection of a GHZ state consists of three stages in an experiment. First, the qubits are initialized using the SWAP-method in Sec. 2.3.3. Secondly, an entanglement stage consisting of two-qubit gates is applied to create a GHZ state. The final step is the characterization of the obtained state. To mimic the experiment, all these stages are implemented in the protocol simulations.

To simulate a distributed qubit register, we take the following two considerations. First, as we were only able to characterize the nuclear spins of a single node (Ch. 3), we assume that there is a symmetry with the other nodes allowing us to use the same set of nuclear spins and their corresponding optimized gates. Furthermore, remote-entanglement links are needed to establish a distributed qubit register over multiple nodes. These links are created by exciting the electron spin during which the spin is in an unknown state. As the nitrogen and electron spin have a hyperfine coupling of 2.186 MHz [19], having the electron spin in an unknown state for 1 ns already completely dephases the nitrogen spin, and any quantum information will be lost. Therefore, we avoid using the nitrogen spin as a qubit because future demonstrations of distributed quantum error correction codes require a lot of electron excitations. However, the nitrogen spin can act as a classical qubit in error correction codes, as demonstrated in Ref. [20].

5.2.1 Single node

The protocol for creating a three qubit GHZ-state on a single node is shown in Fig. 5.1A, which generalizes to an N-qubit GHZ state by attaching two-qubit entangling gates. First, the electron is brought into a superposition state. Then a series of conditional two-qubit gates on the nuclear spin entangles the electron spin with the nuclear spins, resulting in the ideal state:

$$|\mathrm{GHZ}_4\rangle = \frac{1}{\sqrt{2}}(|0--\rangle + |1++\rangle), \tag{5.1}$$

where $|\pm\rangle = \frac{1}{\sqrt{2}}\big(|0\rangle \pm |1\rangle\big)$.

Characterising the quantum state and confirming entanglement

To characterize a quantum state, all the elements of the density matrix need to be measured, which becomes expensive if the number of qubits grows. However, for a GHZ-state with N qubits, there exist 2^N multi-qubit operators that have non-zero expectation values. From measuring the expectation values of this set of operators, the fidelity of the state with the target GHZ-state can be calculated. For example, considering the state $|\Psi_{\mathrm{Bell}}\rangle = \frac{1}{\sqrt{2}}\big(|{+}{+}\rangle + |{-}{-}\rangle\big)$, we obtain the state fidelity by measuring the expectation values of the multi-qubit operators:

$$F = \frac{1 + \langle XX\rangle - \langle YY\rangle + \langle ZZ\rangle}{4}, \tag{5.2}$$

where 1 comes from the expectation value of the idle operator II.

Given the state fidelity for an N-qubit GHZ state, we can determine if the state possesses entanglement by probing an entanglement witness [21]. Here we use the entanglement witness $\mathcal{W} = \mathbb{1} - 2\,|\mathrm{GHZ}_N\rangle\langle\mathrm{GHZ}_N|$. The negativity of the witness confirms multipartite entanglement of the created state. To match the results of the protocol simulations with the experiments as close as possible, we also include a read-out sequence in the simulations, which amounts to applying an extra two-qubit gates for each spin [10]. Hence, we apply an extra error channel to each qubit after the entanglement sequence to simulate the consequence of a read-out sequence.

The resulting register performance is shown in Fig. 5.1B. The maximum GHZ state fidelity reaches only 5 qubits. The limiting factor for this is the large amount of crosstalk of the optimized gates, attributed to spectrally-close spins in the register.

5.2.2 Two node network

To create a qubit-register over two nodes, we consider nodes A and B sharing a remote-entanglement link obtained from Ref. [8]. Both NV spins share one of the two Bell-states $|\Psi^{\pm}\rangle = \frac{1}{\sqrt{2}}(|01\rangle \pm |10\rangle$,

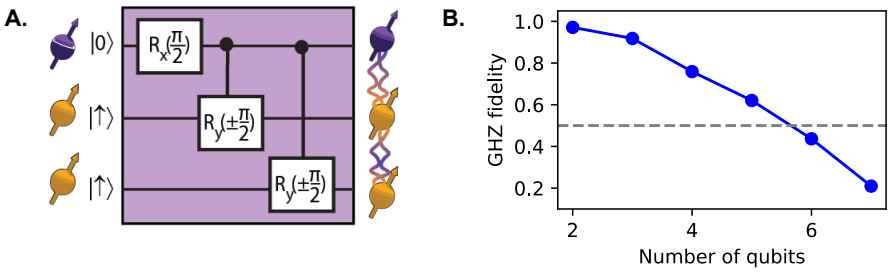

Figure 5.1: **Single node qubit register. A.** Protocol for the creation of a three-qubit GHZ state on a single node. Purple (orange) indicate the electron (carbon) spin initialized with SWAP (Sec. 2.3.3). After the electron set in a superposition state, sequentially applied conditional-$\pi/2$ rotations, generated by the optimized two-qubit gates in Ch. 4, entangle the electron and nuclear spin, creating the GHZ state in Eq. 5.1. **B.** GHZ fidelity as a function of the number of qubits. A state fidelity above 0.5 witnesses multipartite entanglement. This reflects the performance of the qubit register on a single node.

where the first(second) qubit is the NV in node A(B), and $\pm$ depends on which of the photon-detector has clicked. The resulting fidelity of the Bell-state is 0.820(5) with an entangling rate of 9 Hz [8].

By applying local two-qubit gates within each node the entangled state increases over a larger number of qubits. In principle, these local entanglement operations can be placed before or after the remote-entanglement generation. Ref. [8] shows, however, that the coherence of the eigenstates in the computational basis of the nuclear spin is robust to remote-entanglement generation, as opposed to the other cardinal states. Consequently, we time the local entanglement operations after the remote-entanglement generation to protect the coherence. An example of a two-node network protocol where 6 nuclear spins are entangled is shown in Fig. 5.2, which creates a 6-qubit GHZ state:

$$|\text{GHZ}\rangle = \frac{1}{\sqrt{2}}(|01-+-+\rangle \pm |10+-+-\rangle), \tag{5.3}$$

where the last four qubits are the nuclear spins in nodes A and B alternately.

The resulting qubit register performance in Fig 5.2B shows an improvement to the single node register, even though the entangled Bell-state introduces a significant infidelity. We conclude that the advantage of a distributed qubit register is the increased access to higher fidelity gates in both nodes and the reduced sequence time as the entanglement operations on both nodes can happen simultaneously, reducing the effect of natural dephasing of the nuclear spins.

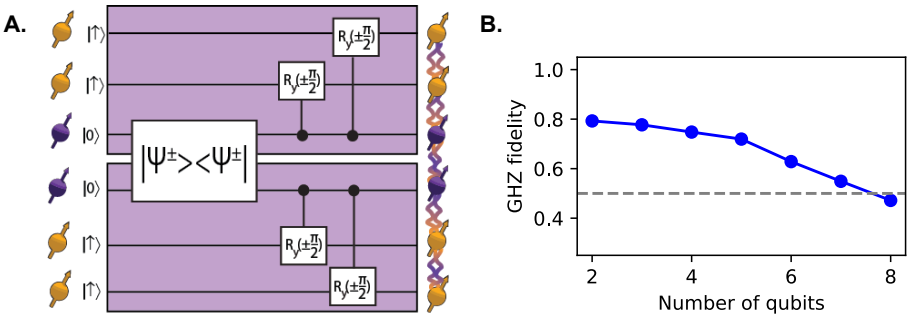

Figure 5.2: **Two node qubit register. A.** Protocol for creating a six-qubit GHZ state distributed over two nodes. The single-photon protocol creates the remote entanglement link (Sec. A.8)[8], entangling the electron spins of both nodes. **B.** GHZ fidelity as a function of the number of qubits. The performance improves as compared with the single node due to the symmetry of the register, as both nodes have access to higher fidelity gates and shorter total sequential time reduces the T_2^* effect.

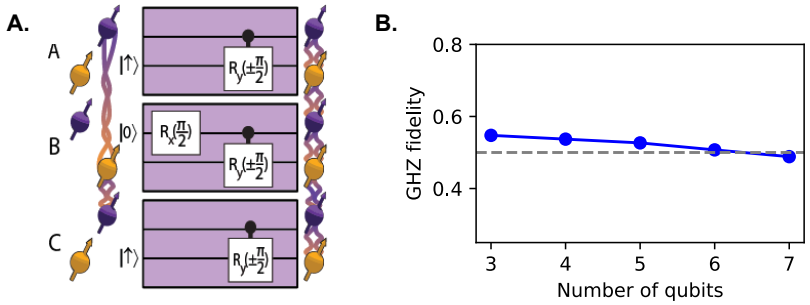

Figure 5.3: **Three node qubit register. A.** Protocol for creating a six-qubit GHZ state distributed over three nodes. **B.** The performance of the qubit register distributed over three nodes.

5.2.3 Three node network

Finally, we explore the performance of a qubit register distributed over three nodes. Ref. [8] has demonstrated a 3 node network by establishing a 3 qubit GHZ-state distributed over the nodes Alice, Bob and Charlie (A, B, C) [8]:

$$|\mathrm{GHZ}\rangle = \frac{1}{\sqrt{2}}\big(\,|0+0\rangle + |1-1\rangle\,\big), \tag{5.4}$$

where from left to right contains the qubits in A, B, C, respectively, and therefore contains a carbon spin in node B [8]. The protocol delivers the GHZ state with a fidelity of 0.538(18) and a rate of 1/(90s), which is a significant increase. However, a longitudinal relaxation time of over 6 minutes is measured [7], concluding that such low entanglement rates do not affect the nuclear spin coherence. Subsequently, having the remote entanglement link, local entanglement operation again increases the size of the GHZ state over the three nodes. The protocol for creating a 6 qubit GHZ state is shown in Fig. 5.3.

The remote entanglement link in Eq. 5.4 contains a carbon spin in node B. To use this node for the qubit register, entanglement between the electron and nuclear spin needs to be created, which would require a two-qubit gate where the control is on the nuclear spin. As there are multiple ways to achieve this, minimizing the total number of applied gates is an important objective to reduce the complexity of the experiment and shorten the total experimental time. Fig. 5.3 shows the approach used in this work, where the electron is put in a superposition state, and then a conditional rotation around the y-axis is applied. Since the $|+\rangle\,/\,|-\rangle$ basis, in which the nuclear spin state is defined, is an eigenbasis of this conditional rotation, the nuclear spin stays untouched while the electron picks up a $\pm\pi/2$-phase depending on the nuclear spin state, consequently entangling with the nuclear spin.

The final ideal GHZ-type state has the form:

$$|\mathrm{GHZ}\rangle = \frac{1}{2}\big(\,|0-\rangle_A\,|(-i)+\rangle_B\,|0-\rangle_C + |1+\rangle_A\,|(+i)-\rangle_B\,|1+\rangle_C\,\big), \tag{5.5}$$

where $|\pm i\rangle = \frac{1}{\sqrt{2}}\big(\,|0\rangle \pm i\,|1\rangle\,\big)$ and for clarity the states are written in electron-carbon order for each node separately. The resulting GHZ-fidelity as a number of qubits is shown in Fig. 5.3. Remarkably, the performance of the qubit register is similar to the single node case.

5.3 Conclusion

In this Chapter, we have built a realistic model for generating GHZ states over a register, that considers all the stages during an experiment and the decoherence sources from Ch. 4, allowing us evaluate the register performance. Using the input from Pompili et al. 2021 [8], we explored the performance of multi-node registers. We simulated a 7 qubit GHZ state over two nodes. The limiting factor is the large amount of crosstalk resulting from spins spectrally-close to each other, as seen in Fig. 3.1 and Tab. A.1. We conclude that multi-node registers increase the access to high-fidelity controllable qubits and lowers the effect of natural dephasing, therefore enabling to counteract the initial infidelity from the remote entanglement-links.

Chapter 6

Conclusion

Future network-based quantum computation requires large qubit registers that can be controlled selectively and deterministically. To realize this, gates are needed that avoid crosstalk and protect the coherence of the system. In this Thesis, we explored the capabilities of DDRF to create large qubit register, developed a new understanding of DDRF and obtained a model to characterize and optimize the gates. Using simulations that considers realistic noise sources, we investigated the performance of a qubit register in a quantum network setting.

The global window approximation, introduced in Ch. 3, provides new knowledge and insight in DDRF, addressing the observed suppression of the efficiency to drive the nuclear spin conditionally in Bradley et al. 2019 [7]. Although this is not an exact solution, we saw that within the regime we are working in the approximation works well. We arrived at this result by a closer inspection of the phase-matching condition of the RF phase with the evolution of the spin, which is the underlying principle of DDRF. Generalizing this to a wide range of RF frequencies reveals the efficiency of DDRF to drive conditionally at different RF frequencies and DDRF parameters. This can be explored for future applications, where by updating the RF phases correctly, the RF frequency can be optimized to enhance the efficiency of a gate, enriching the complexity and potential of DDRF.

The result of the global window enabled to obtain the parameter space that defines the desired operation with DDRF. To optimize the gates, we built a model using the process matrix formalism that estimates the gate fidelity considering the dominant noise sources. This enabled us to characterize regions of high fidelity gates in the parameter space of a nuclear spin, obtaining the gates that minimize the effect of crosstalk and loss of coherence.

To eventually estimate the performance of the qubit register, we built a realistic model that links spins with each other by creating a GHZ state. Employing the high fidelity gates for the set of nuclear spins, we simulated a 7 qubit GHZ state with a fidelity of 0.55 using a qubit-register distributed over two nodes. This outperforms the qubit register on a single node caused by the larger access to high fidelity links, balancing the infidelity generated by the remote-entanglement link. We saw that one of the main limitations hindering the performance of the qubit register is the high amount of crosstalk caused by nuclear spins that are spectrally-close to each other.

One of the main limitations in expanding the qubit register is the amount of crosstalk caused by nuclear spins spectrally-close to each other. The employment of an RF field opens up possibilities to deal with this, such as designing shaped RF-pulses to increase selectivity. Moreover, composite pulses can be exploited to drive multiple spins simultaneously, increasing the efficiency. This, together with the potential to optimize the efficiency using phase-track driving, makes DDRF a promising technique for nuclear spin control in qubit registers.

Acknowledgements

With this, we come to the end of my Thesis. After living 5 years in Groningen, I moved to Delft to do my master thesis at QuTech. It was inspiring to be part of such an exciting and dynamic environment right from day one and I am happy with everything I have learned, both in the fascinating world of quantum physics as well as in doing research.

First of all, I want to thank **Nicolas** for supervising me throughout this project. You are a very warm person, making me welcome from the first day. I admire your positive attitude during the project, which helped me a lot. I wish you best of luck during the rest of your PhD and future!

Tim, thank you for allowing to be part of your group last year. Your enthusiasm and dedication to the research was inspiring during the project, and the questions you asked provided me with a lot of valuable insight.

Also, I want to thank **Benjamin**. I enjoyed the discussions we had. Sharing our excitement for DDRF led to a lot of interesting discussions in front of the whiteboard and were also a lot of fun. Your questions made me rethink critically the work I did.

Caspar, thank you for being my supervisor and your feedback during our meeting in Groningen. And thanks to **Thomas** for reading and evaluating my thesis.

Hans, **Damian**, **Benjamin**, **Guido**, **Jiwon**, **Kai**, **Margriet**, **Christina** and **Laurens** and the rest of Team Diamond, thank you for making last year above all also alot of fun!

The very reason I ended up in Delft is because of **Sjoerd**. Your enthusiasm for the research at QuTech made me excited to take the step. Thanks for all your help throughout the year! Living with you, **Jorn** and **Stijn** the last 7 months were a lot of fun, making return home after long days at the TU always a joy.

Thanks also to **Siddhant**, **Sebastian** and **Boris** for helping me out in the world of quantum process tomography whenever I had questions.

Writing a thesis would have been a completely different experience without all the other students in the *Masterroom*. Discussions, coffeebreaks, lunches and jokes provided always some good refreshment during the day.

A special thanks to my family, **Tineke**, **Marcel**, **Wouter** and **Annemarijn**, for always supporting along every step I took.

Lastly, I would like to thank **Lot**. You had to endure a lot of talk on physics, but I am grateful for all your support!

Appendix A

Appendix

A.1 Table of nuclear spins

	$A_\parallel/2\pi$ [kHz]	$A_\perp/2\pi$ [kHz]
C1	-30.693	-
C2	-45.870	-
C3	20.000	-
C4	19.900	-
C5	18.500	-
C6	-12.570	-
C7	15.744	-
C8	10.020	-
C9	-11.160	-
C10	-7.660	-
C11	4.000	-
C13	-9.000	-
C14	-13.060	-
C15	-6.193	-
C16	-9.500	-

Table A.1: **Hyperfine components of nuclear spins identified using DDRF-spectroscopy.** $A_\parallel$ and $A_\perp$ are the parallel and perpendicular hyperfine interaction components to the applied magnetic field for the nuclear spin of the carbons (Fig. 2.1), that are estimated from the dashed vertical lines Fig. 3.1. These lines correspond to the resonance frequency of the nuclear spin when the electron spin is projected in $m_s = -1$, i.e. $\omega_1 = \sqrt{(\omega_L - A_\parallel)^2 - A_\perp^2}$. At high magnetic field, the contribution of $A_\perp$ is negligible and ω_1 is approximated by $A_\parallel$. In order to fully characterize the hyperfine interaction, $A_\perp$ can be calculated with different methods, such as described in Ref. [7]. However, knowledge of $A_\parallel$ provides good addressing of the nuclear spins.

A.2 Protection of electron coherence

To verify if a particular DD sequence is able to decouple the electron spin from interaction with the nuclear spin-bath, the method described in Abobeih et al. 2018 [15] is employed. Fitting the decay function to the measured electron coherence signal provides a rigorous way to verify if for a particular τ and N the DD sequence is able to protect the electron spin coherence.

Since we only have limited data of the electron coherence as a function of τ, we are not able to fit a decay function and it is difficult to observe a decaying trend due to the noisy data. In an attempt to show that the electron spin suffers no loss in coherence in the bound we set on τ for the parameter space, we analyse our data by calculating the standard deviation for subsets of τ. If the standard deviation stays above 0.95, we conclude that there is no decay in the electron coherence and the subset

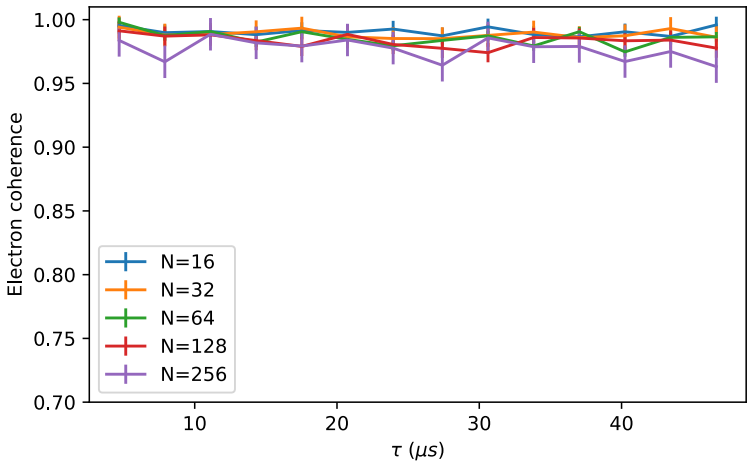

Figure A.1: **Statistical analysis on the electron coherence data.** For each N, the standard deviation of the distribution in the electron coherence for a subset of τ is calculated. Since the standard deviation stays above 0.95 for all τ and N, we conclude that the bounds we set on the parameters space are justified.

of τ is able to protect the electron coherence well. Fig. A.1 shows the result, showing no decay, hence we conclude that the bound we set on $\tau = 50$ μs is justified.

A.3 Harmonics

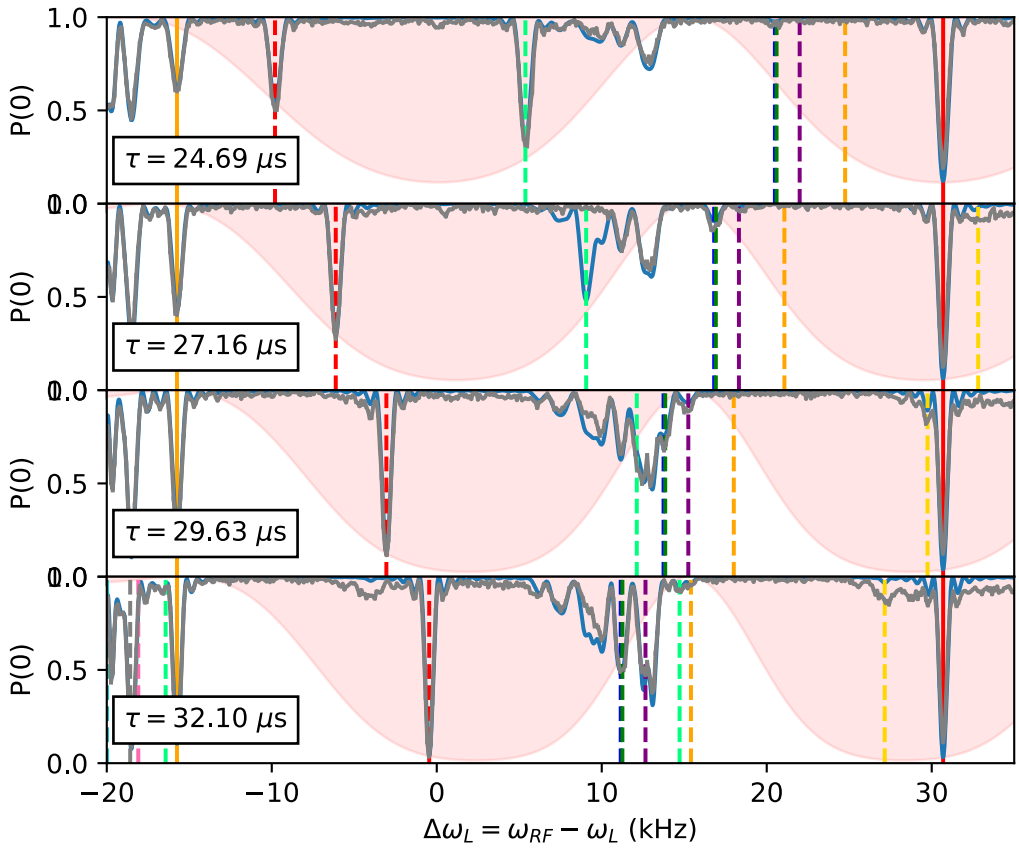

Figure A.2: **Dependence of τ on the position of the harmonics of a nuclear spin.** Results of a DDRF spectroscopy measurement with varying interpulse delay τ, $N = 48$ and $\Omega = 285$ Hz. The dashed lines show the m-th order harmonic $\omega_m = \omega_1 + \frac{\pi m}{\tau}$ of a nuclear spin with resonance frequency ω_1 discussed in Sec. 3.1.1. The shaded area reflect the suppression from the global window of C1, introduced in Sec. 3.2 where each nuclear spin has its own global window. We conclude that the harmonic is a phase-matching condition, hence its efficiency is described by the global window suppression.

A.4 Crosstalk

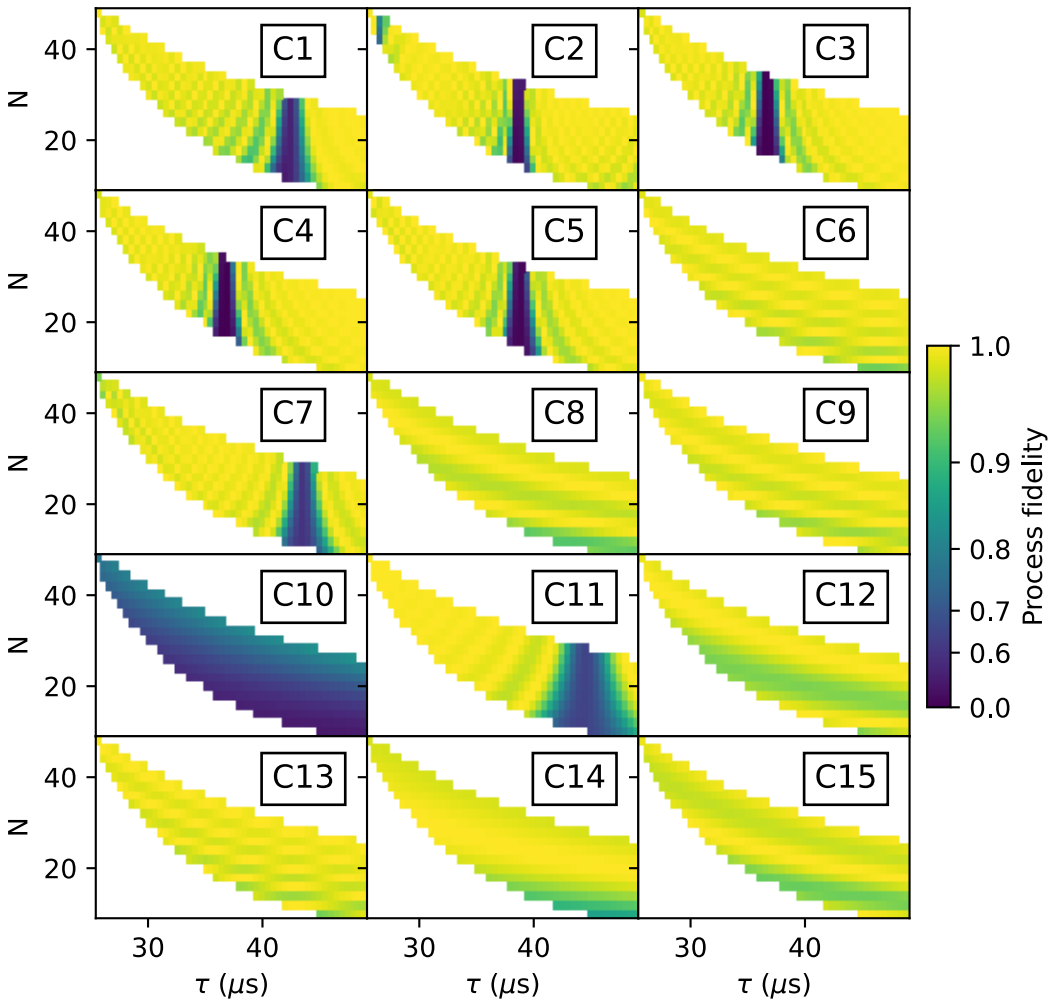

Figure A.3: **The total effect of crosstalk to each nuclear spin from gates on C16.** Crosstalk from a gate is captured by the effect of the gate on all the bystander nuclear spins. Here we calculate the crosstalk effect of C16 on the 15 spins in the register. A decrease in process fidelity with respect to Identity operation indicates crosstalk effects. Two different effects are witnessed. Firstly, is coupling to harmonic of a nuclear spin, which depends on τ. Secondly, the crosstalk induced by spectrally close spins, which happen at gates with broad RF pulses, see C10.

A.5 Nuclear spin dephasing

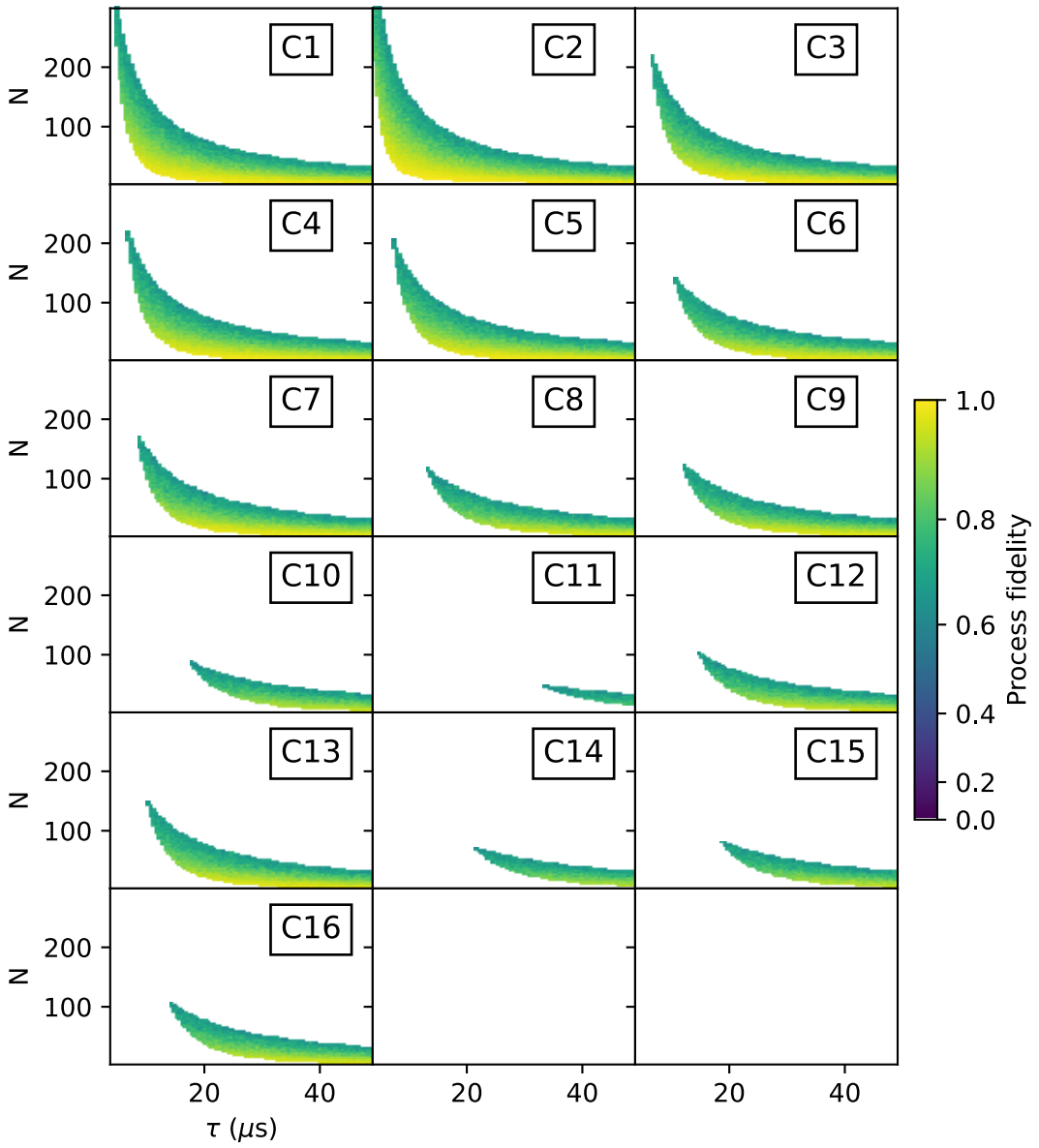

Figure A.4: **Simulations of the effect of nuclear spin dephasing for all the nuclear spins.** The effect of spin-bath on the gate fidelity is simulated with Monte-Carlo methods, where the average gate fidelity reflects the effect of nuclear spin dephasing. The difference in parameter spaces between the nuclear spin comes from the difference in detuning from the Larmor frequency during $m_s = -1$, suppressing the DDRF gates and the number of available gates. We conclude that the effect of the spin-bath scales with total sequence time. Simulations were performed on the DelftBlue High Performance Cluster. [14].

A.6 Gate fidelity

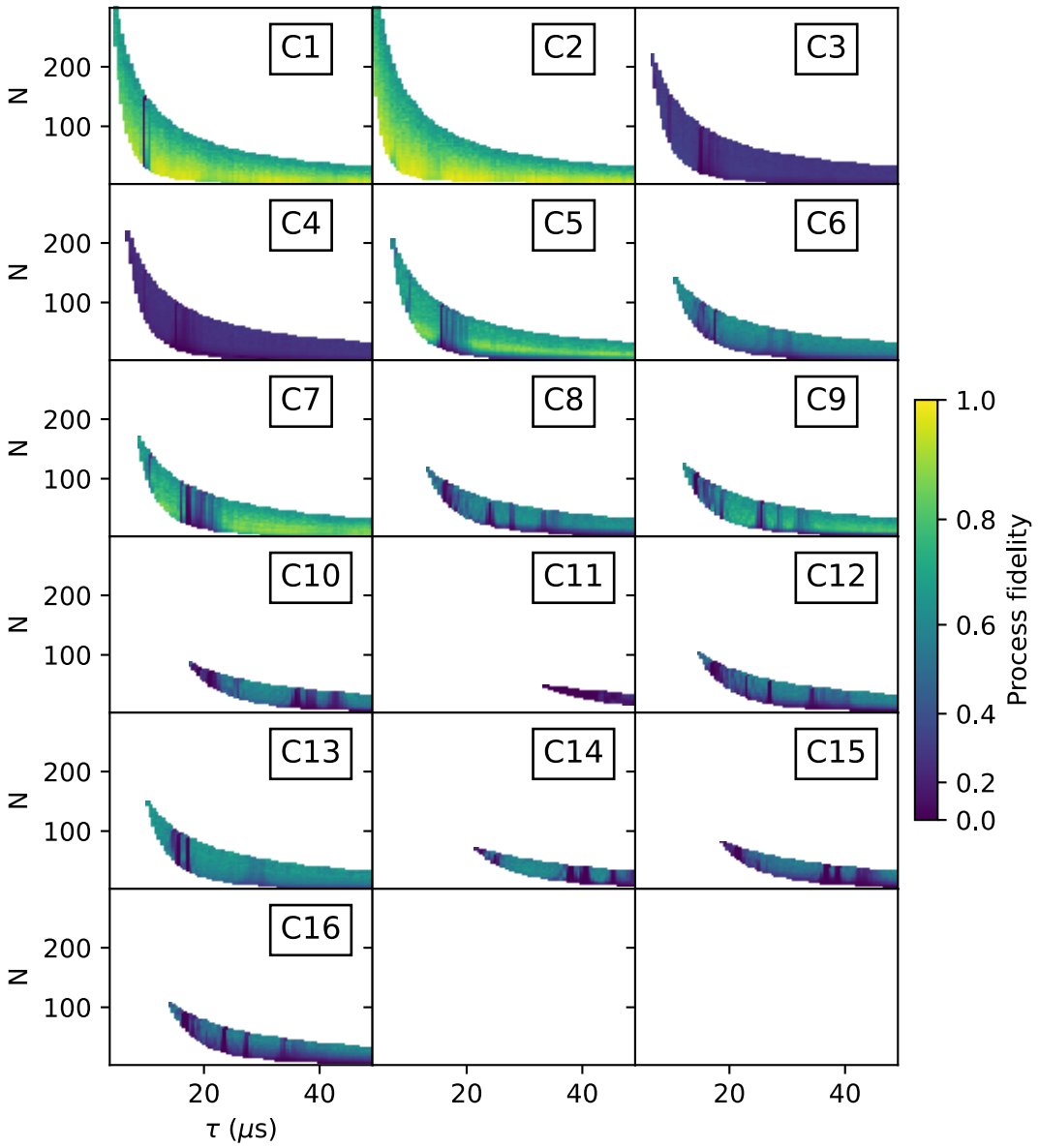

Figure A.5: **Estimate gate fidelity for full parameter space for all nuclear spins.** We conclude that the spin register suffers a lot from crosstalk caused by the nuclear spins spectrally-close to each other, reducing the number of high fidelity gates.

A.7 Process matrix calculation in QuTip

In this Section we elaborate on how the QuTip software package calculates the process matrix χ of a quantum process (e.g. the unitary transformation from a DDRF-gate) as introduced in Sec. 2.4 [12].

The goal is to construct a transformation matrix for a quantum process that describes how the process transforms the density matrix of a system. We can then decompose the transformation in some operator basis that represents how easily interpreted operators contribute to the transformation of an input state.

Considering a process that is described by quantum map $\varepsilon(\rho_{\text{in}}) = \rho_{\text{out}}$, which can be written as:

$$\varepsilon(\rho_{\text{in}}) = \sum_{i}^{d^2} A_i \rho_{\text{in}} A_i^\dagger, \tag{A.1}$$

where d is the number of states of the system (i.e. ρ represented by a $d \times d$ matrix). Given an orthogonal operator basis of our choice $B_{ii}^{d^2}$, which satisfies $\text{Tr}[B_i^\dagger B_j] = d\delta_{ij}$, we can write the map as:

$$\varepsilon(\rho_{\text{in}}) = \sum_{m,n}^{d^2} \chi_{mn} B_m \rho_{\text{in}} B_n^\dagger, \tag{A.2}$$

where $\chi_{mn} = \sum_{ij} b_{im} b_{jn}^*$ and $A_i = \sum_m b_{im} B_m$. Here the χ is the transformation matrix that we are after, and it describes the contribution of $B_m \rho_{\text{in}} B_n^\dagger$ to ρ_{out}.

In a numerical simulation of a quantum process we usally do not have access to the quantum map in Eq. A.1. Instead, what we usually can do is to calculate the propagator U for the density matrix in superoperator form, using the QuTip functions. We can ten write:

$$\varepsilon(\tilde{\rho}_{\text{in}}) = U\tilde{\rho}_{\text{in}} = \tilde{\rho}_{\text{out}}, \tag{A.3}$$

where $\tilde{\rho}$ is the vector representation of the density matrix ρ. If we write Eq. A.2 in superoperator form as well, we obtain:

$$\tilde{\rho}_{\text{out}} = \sum_{m,n}^{d^2} \chi_{mn} \tilde{B}_m \tilde{B}_n^\dagger \rho_{\text{in}} = U\tilde{\rho_{\text{in}}}, \tag{A.4}$$

so we can identify:

$$U = \sum_{mn} \chi_{mn} \tilde{B}_m \tilde{B}_n^\dagger. \tag{A.5}$$

Now this is a linear system of equation for the $d^2 \times d^2$ elements in χ. We can solve it by writing χ and the superoperator propagator as $[d^2]$ vectors and likewise the superoperator product $\tilde{B}_m \tilde{B}_n^\dagger$ as a $[d^4 \times d^4]$ matrix M:

$$U = \sum_{J}^{d^4} M_{ij} \chi_J, \tag{A.6}$$

with the solution:

$$\chi = M^{-1} U. \tag{A.7}$$

Note that to obtain χ with this method, we have to construct the matrix M with a size that is square of the size of the superoperator for the system. Obviously, this scales very badly with increasing system size, but this method can still be very useful for small systems.

A.8 Remote-entanglement generation

In this Section, the protocol for remote entanglement will be explained, i.e. the creation of spin-spin entanglement between distant NV nodes. Before a detailed description will be presented, we give a motivation for the chosen protocol. The protocols that are at hand for remote entanglement generation are probabilistic, meaning that the success rate depends on the probability to detect a photon. The protocol used in this work is the single-photon protocol, which depends on the detection of a single photon to herald remote entanglement. A different protocol that has been used in previous work [22],

is the two-photon protocol [23]. As the detection probability, p_{det}, in the experimental setup that was used in this work is of the order of $10^{-3} - 10^{-4}$, leading to $p_{\text{det}}^2 \ll p_{\text{det}}$. Therefore the single-photon protocol is more favourable to create remote entanglement at a much higher rate as compared to the two-photon protocol. On the other side, the single-photon comes with more complexity and a decrease in fidelity of the delivered entangled state, as will be clear later on.

Single-photon protocol

From now on we will refer to Alice and Bob as two separated NVs centres that we would like to entangle with each other. The single-photon protocol starts by creating spin-photon entanglement for both Alice and Bob. For this, both NVs centres need to be brought into the superposition state:

$$|\Psi\rangle_{A/B} = \sqrt{\alpha_{A/B}}\,|0\rangle + \sqrt{1-\alpha_{A/B}}\,|1\rangle\,, \tag{A.8}$$

where $\alpha_{\text{A/B}}$ is the $|0\rangle$-population for the states in node A and B.

Spin-photon entanglement is then achieved by applying the optical transition introduced above ($|0\rangle \rightarrow |E_{x,y}\rangle$), which decays back to $|0\rangle$ under the emission of a photon if the NV was initially in $|0\rangle$. The presence/absence of a photon then gives the spin-photon entanglement:

$$|\Psi\rangle_{A/B} = \sqrt{\alpha_{A/B}}\,|0\rangle\,|1\rangle_{\gamma} + \sqrt{1-\alpha_{A/B}}\,|1\rangle\,|0\rangle_{\gamma}\,, \tag{A.9}$$

where $|0\rangle_{\gamma}$ ($|1\rangle_{\gamma}$) denotes the absence(presence) of a photon, and is referred to as the flying qubit.

Setting $\alpha = \alpha_A = \alpha_B$ and letting the flying qubits of Alice and Bob interfere at a beam splitter, the which-path information is deleted and the following state is created due to the Hong-Ou-Mandel effect if the flying qubits are indistinguishable:

$$\begin{aligned} |\Psi\rangle_A \otimes |\Psi\rangle_B \rightarrow \quad & \big(\alpha^2/\sqrt{2}\big)\,|0\rangle_A\,|0\rangle_B\,\big(\,|2\rangle_{\gamma,1}\,|0\rangle_{\gamma,2} - |0\rangle_{\gamma,1}\,|2\rangle_{\gamma,2}\,\big) \\ & + \sqrt{(\alpha-\alpha^2)/2}\big(\,|0\rangle_A\,|1\rangle_B + |1\rangle_A\,|0\rangle_B\,\big)\,|1\rangle_{\gamma,1}\,|0\rangle_{\gamma,2} \\ & + \sqrt{(\alpha-\alpha^2)/2}\big(\,|0\rangle_A\,|1\rangle_B - |1\rangle_A\,|0\rangle_B\,\big)\,|0\rangle_{\gamma,1}\,|1\rangle_{\gamma,2} \\ & + \big(1-\sqrt{\alpha}\big)\,|1\rangle_A\,|0\rangle_B\,|1\rangle_{\gamma,1}\,|0\rangle_{\gamma,2}\,, \end{aligned} \tag{A.10}$$

where the subscript for the photon states denotes the photon detector after the beam-splitter.

Unfortunately, the photon detector is not capable of differentiating the number of detected photons. Therefore, by post-selecting on the cases of detecting a photon in one of the photon detectors, the following state is created:

$$\rho_{A\otimes B} = (1-\alpha)\,|\Psi^{\pm}\rangle\,\langle\Psi^{\pm}| + \alpha\,|00\rangle\,\langle 00|_{A,B}\,, \tag{A.11}$$

where the first term is the spin-spin entangled state $|\Psi^{\pm}\rangle = \frac{1}{\sqrt{2}}\big(\,|0\rangle_A\,|1\rangle_B \pm e^{i\Delta\theta}\,|1\rangle_A\,|0\rangle_B\,\big)$ depending on the phase difference $\Delta\theta$ between both flying qubits, which then depends on the differences in optical paths that both flying qubits have traversed. The last term is an unentangled state, and therefore imposes a source of infidelity due to the double-excitation of the NV centres.

From this, it is seen that the phase difference $\Delta\theta$ affects the fidelity of the Bell states. In order to minimize the effect, the phase difference needs to be stabilized. A novel stabilization scheme is presented in Ref. [8].

If assuming $p_{det} = p_{det}^A = p_{det}^B$ with $p_{det}^2 \ll p_{det}$ and $\alpha = \alpha_A = \alpha_B$, the probability per attempt to successfully herald an entangled state is $2\alpha p_{det}$. This results in a generation rate of 10 Hz, as opposed to 10 mHz for the two-photon protocol [23]. On the other hand, the downside of this scheme is that the maximum fidelity of the delivered entangled state is $F = 1 - \alpha$, i.e. limited by the probability that one of the two photons emitted by the nodes is not detected due to being lost or because of double-excitation.

A.9 Controlling individual nuclear spins using dynamical decoupling

By using a dynamical decoupling sequence of the form $(\tau - \pi - 2\tau - \pi - \tau)$, where π-pulses on the electron follow each other after a specific waiting time τ, the electron spin is decoupled from

oscillating magnetic fields that are off-resonant from the interpulse frequency $1/(2\tau)$. In other words, the dynamical decoupling sequences isolate the interaction of the electron spin with an oscillating magnetic field that does have a frequency equal to the interpulse frequency. It is shown in Ref. [6] that by setting the interpulse delay to the resonance condition for a specific nuclear spin:

$$\tau_k = \frac{(2k-1)\pi}{2\omega_0 - A_\parallel}, \tag{A.12}$$

with integer $k > 0$, the interaction Hamiltonian of Eq. 2.8 is recovered.

The unitary evolution operator for one DD sequence then becomes:

$$V_0 = e^{-iH_0\tau} e^{-iH_1 2\tau} e^{-iH_0\tau} \tag{A.13}$$

$$V_1 = e^{-iH_1\tau} e^{-iH_0 2\tau} e^{-iH_1\tau}, \tag{A.14}$$

where the subscripts indicate the different unitary evolutions under different initial electron eigenstates. These unitaries can be rewritten as single-qubit rotations:

$$V_0 = e^{-i\phi(\mathbf{I}\cdot\hat{\mathbf{n}}_0)} \tag{A.15}$$

$$V_1 = e^{-i\phi(\mathbf{I}\cdot\hat{\mathbf{n}}_{-1})}, \tag{A.16}$$

where $\hat{\mathbf{n}}_0(\hat{\mathbf{n}}_{-1})$ is the rotation axis of the nuclear spin for $m_s = 0(-1)$ and ϕ is the rotation angle for one DD sequence.

The rotation axes will be anti-parallel when τ is set to Eq. A.12 and results in non-trivial rotations. The rotation angle ϕ will then be dependent on the number of π-pulses N. By selecting specific combinations of these parameters, it is then possible to design two-qubit gates.

Note a few important features about this method. First, the selectivity of this method (i.e. how well it is possible to address a single nuclear spin) is dependent on the spectral isolation of the nuclear spin. In other words, if a specific τ overlaps with multiple nuclear spins, it is only possible to address a nuclear spin individually by choosing higher resonances of a particular spin, but this will also impose an increasing gate time. Second, this method works best for larger hyperfine couplings, since these are more rare, therefore spectrally isolated. Third, Eq. 2.8 shows that large $A_\perp$ induces more rotation per DD sequence, since this tilts the rotation axis more during evolution in $m_s = -1$. This relates to faster gates.

Bibliography

[1] Gordon E Moore. "Cramming More Components onto Integrated Circuits". en. In: *PROCEEDINGS OF THE IEEE* 86.1 (1998).

[2] R. P. Feynman. "Simulating Physics with Computers". In: *International Journal of Theoretical Physics* 21.6 (1982), pp. 467–488.

[3] Y. Cao, J. Romero, and A. Aspuru-Guzik. "Potential of quantum computing for drug discovery". In: *IBM Journal of Research and Development* 62.6 (Nov. 2018). Conference Name: IBM Journal of Research and Development, 6:1–6:20. ISSN: 0018-8646. DOI: 10.1147/JRD.2018.2888987.

[4] Aram W. Harrow, Avinatan Hassidim, and Seth Lloyd. "Quantum Algorithm for Linear Systems of Equations". In: *Physical Review Letters* 103.15 (Oct. 2009). Publisher: American Physical Society, p. 150502. DOI: 10.1103/PhysRevLett.103.150502. URL: https://link.aps.org/doi/10.1103/PhysRevLett.103.150502 (visited on 02/04/2023).

[5] Michiel Bakker. *Frozen Core Spin Dynamics in Diamond*. MSc thesis 2015.

[6] T. H. Taminiau et al. "Detection and control of individual nuclear spins using a weakly coupled electron spin". In: *Physical Review Letters* 109.13 (Sept. 2012). arXiv:1205.4128 [cond-mat, physics:quant-ph], p. 137602. ISSN: 0031-9007, 1079-7114. DOI: 10.1103/PhysRevLett.109.137602. URL: http://arxiv.org/abs/1205.4128 (visited on 10/26/2022).

[7] C. E. Bradley et al. "A Ten-Qubit Solid-State Spin Register with Quantum Memory up to One Minute". In: *Phys. Rev. X* 9 (3 Sept. 2019), p. 031045. DOI: 10.1103/PhysRevX.9.031045. URL: https://link.aps.org/doi/10.1103/PhysRevX.9.031045.

[8] Matteo Pompili et al. "Realization of a multi-node quantum network of remote solid-state qubits". In: *Science* 372.6539 (Apr. 2021). arXiv:2102.04471 [quant-ph], pp. 259–264. ISSN: 0036-8075, 1095-9203. DOI: 10.1126/science.abg1919. URL: http://arxiv.org/abs/2102.04471 (visited on 08/09/2022).

[9] H. J. Kimble. "The quantum internet". en. In: *Nature* 453.7198 (June 2008). Number: 7198 Publisher: Nature Publishing Group, pp. 1023–1030. ISSN: 1476-4687. DOI: 10.1038/nature07127. URL: https://www.nature.com/articles/nature07127 (visited on 02/04/2023).

[10] M.H.M.A. Abobeih. "From atomic-scale imaging to quantum fault-tolerance with spins in diamond". en. PhD thesis. Delft University of Technology, 2021. DOI: 10.4233/UUID:CCE8DBCB-CFC2-4FA2-B78B-99C803DEE02D. URL: http://resolver.tudelft.nl/uuid:cce8dbcb-cfc2-4fa2-b78b-99c803dee02d (visited on 08/09/2022).

[11] Man-Duen Choi. "Completely positive linear maps on complex matrices". en. In: *Linear Algebra and its Applications* 10.3 (June 1975), pp. 285–290. ISSN: 0024-3795. DOI: 10.1016/0024-3795(75)90075-0. URL: https://www.sciencedirect.com/science/article/pii/0024379575900750 (visited on 01/15/2023).

[12] J. R. Johansson, P. D. Nation, and Franco Nori. "QuTiP 2: A Python framework for the dynamics of open quantum systems". In: *Computer Physics Communications* 184.4 (Apr. 2013). Publisher: Elsevier BV, pp. 1234–1240. DOI: 10.1016/j.cpc.2012.11.019. URL: https://doi.org/10.1016%2Fj.cpc.2012.11.019.

[13] John. *Don't invert that matrix*. en-US. Jan. 2010. URL: https://www.johndcook.com/blog/2010/01/19/dont-invert-that-matrix/ (visited on 01/21/2023).

[14] Delft High Performance Computing Centre (DHPC). *DelftBlue Supercomputer (Phase 1)*. 2022. URL: https://www.tudelft.nl/dhpc/ark:/44463/DelftBluePhase1.

[15] M. H. Abobeih et al. "One-second coherence for a single electron spin coupled to a multi-qubit nuclear-spin environment". en. In: *Nature Communications* 9.1 (Dec. 2018), p. 2552. ISSN: 2041-1723. DOI: 10.1038/s41467-018-04916-z. URL: http://www.nature.com/articles/s41467-018-04916-z (visited on 08/06/2022).

[16] Peter C. Humphreys et al. "Deterministic delivery of remote entanglement on a quantum network". en. In: *Nature* 558.7709 (June 2018), pp. 268–273. ISSN: 0028-0836, 1476-4687. DOI: 10.1038/s41586-018-0200-5. URL: http://www.nature.com/articles/s41586-018-0200-5 (visited on 08/05/2022).

[17] H. P. Bartling et al. *Coherence and entanglement of inherently long-lived spin pairs in diamond*. arXiv:2103.07961 [quant-ph]. Mar. 2021. URL: http://arxiv.org/abs/2103.07961 (visited on 01/27/2023).

[18] Alexander N. Korotkov. *Error matrices in quantum process tomography*. arXiv:1309.6405 [quant-ph]. Nov. 2013. URL: http://arxiv.org/abs/1309.6405 (visited on 12/13/2022).

[19] H. Bernien. "Control, measurement and entanglement of remote quantum spin registers in diamond". en. In: (2014). URL: https://repository.tudelft.nl/islandora/object/uuid%3A75130c37-edb5-4a34-ac2f-c156d377ca55 (visited on 01/27/2023).

[20] M. H. Abobeih et al. "Fault-tolerant operation of a logical qubit in a diamond quantum processor". en. In: *Nature* 606.7916 (June 2022). Number: 7916 Publisher: Nature Publishing Group, pp. 884–889. ISSN: 1476-4687. DOI: 10.1038/s41586-022-04819-6. URL: https://www.nature.com/articles/s41586-022-04819-6 (visited on 01/27/2023).

[21] Otfried Gühne and Géza Tóth. "Entanglement detection". en. In: *Physics Reports* 474.1 (Apr. 2009), pp. 1–75. ISSN: 0370-1573. DOI: 10.1016/j.physrep.2009.02.004. URL: https://www.sciencedirect.com/science/article/pii/S0370157309000623 (visited on 01/24/2023).

[22] B. Hensen et al. "Loophole-free Bell test using electron spins in diamond: second experiment and additional analysis". In: *Scientific Reports* 6.1 (Aug. 2016). DOI: 10.1038/srep30289. URL: https://doi.org/10.1038%2Fsrep30289.

[23] Sean D. Barrett and Pieter Kok. "Efficient high-fidelity quantum computation using matter qubits and linear optics". In: *Physical Review A* 71.6 (June 2005). DOI: 10.1103/physreva.71.060310. URL: https://doi.org/10.1103%2Fphysreva.71.060310.